Marine Minerals Administration
Oil Spill Preparedness Division
Bridging the Gap Between the Dispersion Effectiveness at Various Scales

Final Report

August 2026

Michel Boufadel, Fangda Cui, Zhaonian Qu, Elie Khoury, and Wen Ji

US Department of the Interior
Marine Minerals Administration
Oil Spill Preparedness Division

Bridging the Gap Between the Dispersion Effectiveness at Various Scale

Final Report

OSRR # 1143

August 2026

Authors:
Michel Boufadel
New Jersey Institute of Technology

Fangda Cui
New Jersey Institute of Technology

Zhaonian Qu
New Jersey Institute of Technology

Elie Khoury
New Jersey Institute of Technology

Wen Ji
New Jersey Institute of Technology
Prepared under 140E0124P0016
By
New Jersey Institute of Technology
323 DR MARTIN LUTHER KING JR
BLVD, NEWARK, NJ 07102

US Department of the Interior
Marine Minerals Administration
Oil Spill Preparedness Division

DISCLAIMER

Study concept, oversight, and funding were provided by the US Department of the Interior (DOI), Marine Minerals Administration (MMA), Oil Spill Preparedness Division (OSPD), Sterling, VA, under Contract Number 140E0124P0016. This report has been technically reviewed by MMA, and it has been approved for publication. The views and conclusions contained in this document are those of the authors and should not be interpreted as representing the opinions or policies of the US Government, nor does mention of trade names or commercial products constitute endorsement or recommendation for use.

REPORT AVAILABILITY

The PDF file for this report is available through the following sources. Click on the URL and enter the appropriate search term to locate the PDF:

Document Source	Search Term	URL
Marine Minerals Administration (MMA)	Project Number – 1143	https://www.bsee.gov/what-we-do/research/oil-spill-preparedness/oil-spill-response-research
U.S. Department of the Interior Library	Bridging the Gap Between the Dispersion Effectiveness at Various Scale	https://library.doi.gov/uhtbin/cgisirsi/?ps=8L0mpW5uPV/SIRSI/X/60/495/X
National Technical Reports Library	Bridging the gap	https://ntrl.ntis.gov/NTRL/

Sources : a) MMA (2019), b) DOI [2021], c) National Technical Information Service (2021)

CITATION

Boufadel, M.C., Cui, F., Qu, Z., Khoury, E., and Ji., W (NJIT, Newark NJ), 2026. Bridging the Gap Between the Dispersion Effectiveness at Various Scale: US Department of the Interior, Marine Minerals Administration. 63 p. Contract No.: 140E0124P0016. https://doi.org/10.70149/H9LIFYSIF7AO

ABOUT THE COVER

Cover image by Dr. Gina Coelho. OSPR Project 1143 – “Bridging the Gap Between the Dispersion Effectiveness at Various Scale”. The oil breakup under breaking wave test at Ohmsett tank, New Jersey.

ACKNOWLEDGEMENTS

This research was funded by the Marine Minerals Administration (MMA).

MMA OSPD PUBLIC POSTING APPROVAL SHEET

1. Report Date: (DD-MM-YYYY)

31-08-2026

2. REPORT TYPE: (Interim for peer review, Final, etc.)
Final Report

3. START DATE: (DD-MM-YYYY)	**4. END DATE: (DD-MM-YYYY)**
01-07-2024	**31-08-2026**

5. TITLE:

Bridging the Gap Between the Dispersion Effectiveness at Various Scales

6. CONTRACT/IAA NUMBER:

140E0124P0016

7. OIL SPILL RESPONSE RESEARCH PROJECT NUMBER:

1143

8. PERFORMING ORGANIZATION NAME(S) AND ADDRESS(ES):

New Jersey Institute of Technology, 323 Dr Martin Luther King Jr BLVD, Newark, NJ 07102

9. AUTHOR(S):

Michel Boufadel, Fangda Cui, Zhaonian Qu, Elie Khoury, Wen Ji

10. DISTRIBTION/AVAILABILITY STATEMENT (INDICATE PUBLIC AVAILABILIY OR DISTRIBTION LIMIATIONS OF THE REPORT: (e.g., PROPRIETARY)

Publicly Available

11. SUPPLEMENTARY NOTES:

12. ABSTRACT: (BRIEF, 200 WORD, FACTUAL SUMMARY OF THE MOST SIGNIFICANT INFORMATION)

Dispersion effectiveness (DE) is a means of measuring the ability of dispersants to enhance the tendency for natural dispersion of oil into the water column. Understanding the DE of spilled oil in marine environments is a necessary aspect of predicting the transportation and fate of spilled materials. In the absence of studying crude oil spill in marine environments, scaled models, at the wave tank and laboratory scales, have been employed to predict DE. To better understand the conditions at each scale, researchers have characterized the hydrodynamics in the laboratory scale vessels (example: baffled flasks) and wave tanks (example: Ohmsett); however, the scalability between systems is a challenge due to the complexity of the apparatus and the disparity in systems. As a result, laboratory scale DE measurements could not be directly correlated to DE measurements at test tank or ocean scales. Identifying the necessary parameters, such as energy dissipation rate and dilution, was needed to model dispersion effectiveness across scales. The goal of this project was to understand the physics and develop a model correlating the formation and transport of oil droplets across scales, from laboratory, to wave tank, and finally ocean scale. Data from previous laboratory and Ohmsett tank experiments were used as a basis for the model development. This modeling effort was completed through a contract with the New Jersey Institute of Technology, with a value of $363,389.

Modeling results using VDROP identified the critical variables needed to scale DE. Required inputs to model droplet size distribution, and therefore dispersant effectiveness, are the interfacial tension (based on the dispersant-to-oil ration), oil viscosity, and energy dissipation rates based on ocean conditions. This model allows for more accurate predictions of the droplet size distribution of a target oil in specific sea states. Responders will be able to more accurately predict crude oil transport and dissipation into the water column with and without dispersant applications and ultimately predict the fate of spilled crude oil.

13. KEY WORDS/PHRASES: **Dispersants, Dispersant to Oil Ratio, Droplet Size Distribution, Baffled Flask Test, Diffusivity**	
14. CONTRACTING OFFICER REPRESENTATIVE: **Kevin Cabaniss**	**15. PHONE NUMBER/EMAIL ADDRESS:** **703-787-1120, kevin.cabaniss@bsee.gov**
16. APPROVER: (Branch Manager) **Karen Stone**	**17. PHONE NUMBER/EMAIL ADDRESS:** **703-787-1810, karen.stone@bsee.gov**

GRAPHICAL ABSTRACT

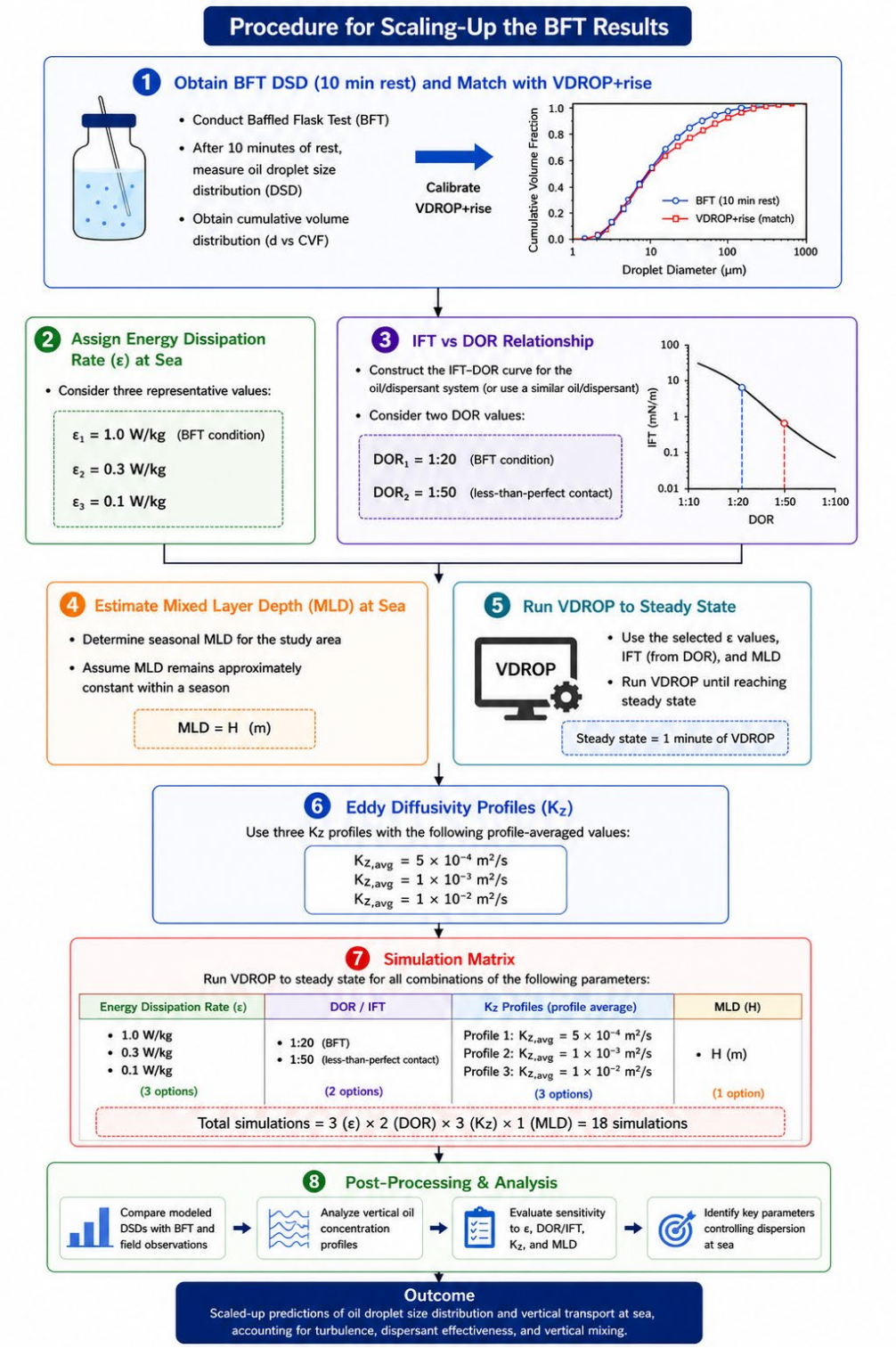

EXECUTIVE SUMMARY

Dispersant effectiveness (DE) tests are routinely used to evaluate the ability of chemical dispersants to enhance the dispersion of oil into the water column. However, significant differences exist between DE measurements in laboratory-scale tests, wave-tank experiments, and actual ocean conditions. As a result, dispersant effectiveness measured in one system cannot always be directly translated to another. The objective of this study was to develop a physics-based framework that links oil droplet formation and transport processes across these different scales and improves the prediction of dispersant effectiveness under field conditions. To accomplish this objective, results at the laboratory scale - Baffled Flask Test (BFT) were obtained and analyzed along with wave-tank breaking-wave experiments conducted at the Ohmsett, without and with dispersant. The investigation relied on using computational fluid dynamics (CFD), droplet formation and transport simulations.

Laboratory baffled flask experiments were performed using weathered Alaska North Slope crude oil at dispersant-to-oil ratios of 0:0 (no dispersant), 1:20 and 1:50. The 1:20 and 1:50 results had a large portion of droplets smaller than 5 microns suggesting that tip-streaming, whereby the oil breaks off the droplets in form of micron sized filaments, was a major mechanism. For this reason, the droplet formation model VDROP was run with the tip-streaming module, and the fit to the data allowed estimating relevant parameters that could be used in scaling up.

The Ohmsett experiments were conducted using weathered Hibernia oil during the year 2021 in a project funded by the Canadian government. The experiments manifested clear differences between untreated and dispersant-treated oil. Untreated oil formed droplets primarily in the hundreds-of-micrometers (i.e., microns) to millimeter size range, while dispersant-treated oil generated dense plumes of micron-sized droplets. The work within this project entailed conducting CFD simulations to characterize the wave breaker and predict the resulting oil DSD. Large-eddy simulation (LES) models were run to reproduce the hydrodynamics of plunging breakers observed in the Ohmsett experiments. The simulations successfully reproduced water-surface elevations, velocity fields, and vorticity distributions measured during the experiments. The LES results provided estimates of turbulent energy dissipation rates and eddy diffusivities throughout the breaking process, supplying hydrodynamic information that is difficult or impossible to obtain from field measurements alone. The CFD simulations (i.e., LES) were coupled with the VDROP population balance model to predict oil droplet size distributions.

The project also examined the relationship between the spatial distribution of oil droplets and dispersant effectiveness under ocean conditions. A one-dimensional transport model was developed to simulate the combined effects of droplet buoyancy and turbulent diffusion in the Mixed Layer of the ocean (30 to 100 m). The model assumed that the droplet size distribution (DSD) may be obtained from a droplets model, such as VDROP. The simulations demonstrated that, in general conditions, droplets larger than 100 microns resurface within minutes, and that droplets less than 50 microns are most impacted by ocean diffusion.

Based on these findings, it was concluded that knowledge of the oil DSD is a critical step for scaling up (or down) results. The DSD depends on the interfacial tension (IFT) (which depends on the dispersant to oil ratio (DOR)), oil viscosity, and the energy dissipation rate. Therefore, knowledge of these three parameters in any environment produces the DSD. The energy dissipation rate may be obtained based on the sea state, and one needs to consider ranges of this parameter, and not only point estimates. The vertical transport of oil depends on oil density (buoyancy) and turbulent diffusion, and the latter needs to be estimated based on the hydrodynamics of the vessel under consideration, a baffled flask, a wavetank, or the ocean. An expression for the eddy diffusivity (or diffusion coefficient) based on sea state was utilized, and three conditions representing a highly agitated sea down to a relatively calm sea with small waves were considered. Also important is the relation between the IFT and the DOR, and we are recommending that one develops it based on the oil of interest. This is because one needs to consider situations where the ideal DOR, for example 1:20, might not be achieved at sea. By providing the IFT to a droplet model, such as VDROP, and based on hydrodynamics at sea, one may obtain the DSD and droplet transport within the water column.

Contents

List of Figures

List of Tables

1 Introduction

Chemical dispersants are used as an oil spill response strategy to enhance the natural dispersion of spilled oil into the water column. By reducing the oil–water interfacial tension (IFT), dispersants promote the breakup of surface oil slicks into smaller droplets that can be transported and diluted by ocean turbulence. The effectiveness of dispersant applications is commonly evaluated through dispersant effectiveness (DE) tests conducted under controlled laboratory conditions, as well as wave tank (mesocosm scale) studies. Although these testing methods provide valuable information regarding dispersant performance, extrapolating the results to field conditions remains difficult because of differences in hydrodynamic conditions, turbulence characteristics, and spatial and temporal scales.

A major limitation in evaluating dispersant performance is the scalability of experimental observations. Laboratory vessels typically have characteristic dimensions on the order of centimeters, whereas wave tanks may extend tens of meters, and field conditions encompass spatial scales of hundreds of meters. The small spatial scales have associated with their temporal scales. As a result, direct comparison of dispersant effectiveness measurements among different systems is often problematic. Previous studies have shown that oil droplet formation and dispersion depend strongly on several key parameters, including oil properties, the dispersant to oil ratio (DOR), the turbulent energy dissipation rate, the mixing duration, and turbulent diffusion (which leads to dilution). These factors collectively determine the resulting oil droplet size distribution (DSD), which is a fundamental variable impacting oil transport and fate.

Numerical modeling provides a means of unifying the approach to understanding experimental observations across scales and factors. Computational fluid dynamics (CFD) models can resolve the hydrodynamic processes responsible for oil entrainment and turbulent mixing, while population balance models such as the VDROP model developed by the Boufadel group (Zhao et al., 2014) can simulate droplet breakup and coalescence processes to predict evolving DSD. By coupling hydrodynamic simulations with droplet population dynamics, physically based relationships can be established between laboratory-scale measurements, wave-tank observations, and field-scale oil dispersion processes.

Large-scale breaking-wave experiments conducted at the Ohmsett facility have provided valuable datasets for investigating oil dispersion under realistic wave-breaking conditions. These experiments have demonstrated that dispersant-treated oil can generate substantial populations of micron-sized droplets that are not always adequately represented by existing droplet breakup models. Laboratory-scale baffled flask experiments further indicate that reductions in oil–water interfacial tension can lead to breakup mechanisms beyond conventional turbulent fragmentation, in a process known as tip-streaming whereby oil sloughs tiny droplets. Improved representation of these mechanisms is therefore necessary for accurately predicting DSD under dispersant-treated conditions.

The droplet size impacts the fate and transport of dispersed oil in the ocean. Smaller droplets exhibit lower buoyant rise velocities and are therefore more likely to remain suspended within the ocean mixed layer due to turbulent mixing, whereas larger droplets tend to resurface more rapidly. Consequently, the vertical transport and retention of dispersed oil droplets influence both the persistence of oil within the water column and the effectiveness of dispersion. In addition, the

longer a droplet stays submerged, the more it dissolves in the water column and the higher the chance is for it to biodegrade (i.e., gets uptaken by microorganisms).

The present study aimed to integrate laboratory-scale baffled flask measurements, meso-scale Ohmsett experiments and CFD simulation (LES), an enhanced VDROP population balance framework, and simulations of oil transport within the ocean mixed layer. Hydrodynamic conditions within the experimental systems were characterized and linked to oil droplet formation processes through physically based breakup models. In addition, a tip-streaming mechanism was incorporated into the VDROP framework to improve predictions under low-IFT conditions representative of dispersant-treated oil. The resulting modeling framework was evaluated against measured droplet size distributions (DSD) obtained from both laboratory and wave-tank experiments. Predicted droplet size distributions were subsequently coupled with mixed-layer transport simulations to investigate the vertical retention of dispersed oil and to identify conditions under which oil droplets may be considered effectively dispersed. By improving the representation of oil droplet formation, breakup, transport, and retention processes, this study seeks to support the development of more reliable oil spill fate and transport models, strengthen the scientific basis for dispersant response decisions, and provide a framework for evaluating dispersant effectiveness under field conditions.

2 Objectives

The objective of this study was to develop and validate a physics-based modeling framework for predicting oil droplet size distributions and dispersant effectiveness across laboratory, wave-tank, and field-relevant conditions. Building upon previous efforts to address scaling challenges among dispersant effectiveness testing systems, the study integrated large-scale Ohmsett breaking-wave experiments, laboratory-scale baffled flask experiments, computational fluid dynamics (CFD) simulations, population balance modeling, and upper-ocean transport modeling.

Particular emphasis was placed on quantifying the effects of turbulent energy dissipation, mixing duration, dilution processes, oil properties, and oil–water interfacial tension on oil droplet formation, breakup, and transport. Experimental measurements were used to calibrate and validate the numerical models, including the large-eddy simulation (LES) framework and the population balance model (PBM). The LES simulations were employed to reproduce the hydrodynamics of breaking waves and provide detailed information on velocity fields, turbulence structures, vorticity generation, eddy diffusivity, and energy dissipation rates that cannot be obtained directly from measurements alone. These hydrodynamic parameters were subsequently linked to oil droplet breakup and transport processes through the population balance framework. A modified VDROP model incorporating tip-streaming mechanisms was developed and evaluated to improve predictions of micron-sized oil droplets generated under dispersant-treated conditions. In addition, a vertical advection–diffusion framework was applied to investigate the transport and retention of dispersed oil droplets within the ocean mixed layer and to examine the relationship between droplet size distributions and dispersant effectiveness under ocean conditions.

The overall goal of the study was to establish physically based relationships among laboratory-scale measurements, wave-tank observations, and field-scale oil dispersion processes, thereby improving the capability of oil spill fate and transport models to predict oil droplet size distributions, dispersed oil retention, and dispersant effectiveness across multiple spatial scales.

To achieve the objectives four complementary methodologies were employed. These included laboratory-scale baffled flask experiments; droplet formation using a droplet population balance model, VDROP; wave tank experiments conducted at Ohmsett, New Jersey; and high-fidelity computational fluid dynamics (CFD) simulations. Together, these approaches provided a comprehensive framework for investigating oil droplet formation, transport, and fate under a range of environmental and operational conditions.

3 Lab Scale, Baffled Flask

3.1 Experiments

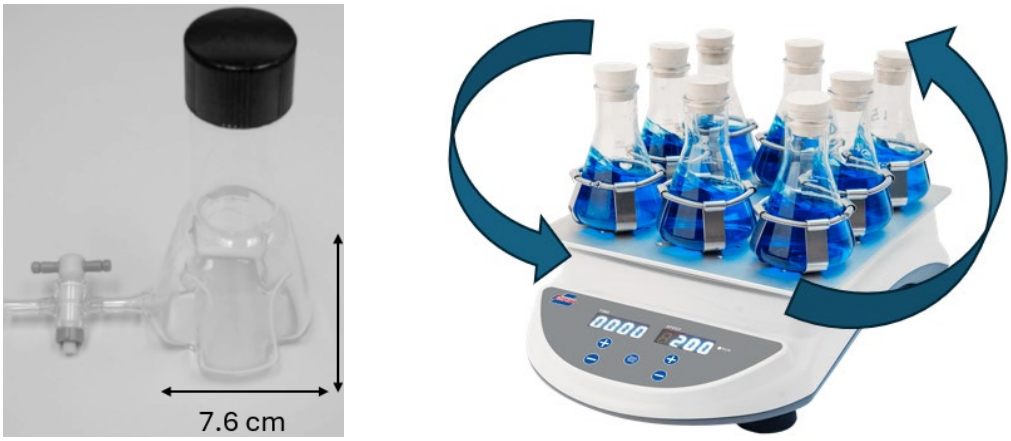

(a) (b)

Figure. 3.1.1 The baffled flask (a) and orbital shaker (b) used for laboratory-scale oil dispersion tests

The baffled flask test (BFT) was conducted following a laboratory-scale dispersant effectiveness protocol (ASTM International 2026; U.S. Environmental Protection Agency 2024). Briefly, 120 mL of artificial seawater (salinity around 32.0 g/L) is placed in a baffled flask (Figure. 3.1.1a), and 80 mg of oil (approximately 90 µL) are added on the water surface. For dispersant-treated cases, approximately 4 µL of dispersant, Corexit 9500, is added to achieve the target dispersant-to-oil ratio (DOR) of 1:20. The flask is then subjected to controlled mixing (200 rpm) for 10 minutes using an orbital shaker (Figure. 3.1.2b) to simulate turbulent energy dissipation and oil dispersion processes that occur under field conditions. Following the mixing period, the flask is allowed to remain undisturbed for 10 min. After the settling period, a water sample is collected from the bottom of the flask through a spigot for analysis. In the EPA protocol, the concentration in the water sample is used to compute the submerged (called also dispersed) mass of oil and the ratio of the dispersed mass to the nominal mass provides the dispersion effectiveness in percent.

For the current project, we used the sample from the bottom to measure the oil droplet size distribution using a LISST 200 (LISST-100X, Sequoia Scientific Inc., Bellevue, WA, USA), which provides the sizes from 2.0 microns up to 461 microns in a geometric progression. The measured DSDs are needed to calibrate the droplet model VDROP, a necessary step to scale up the BFT results.

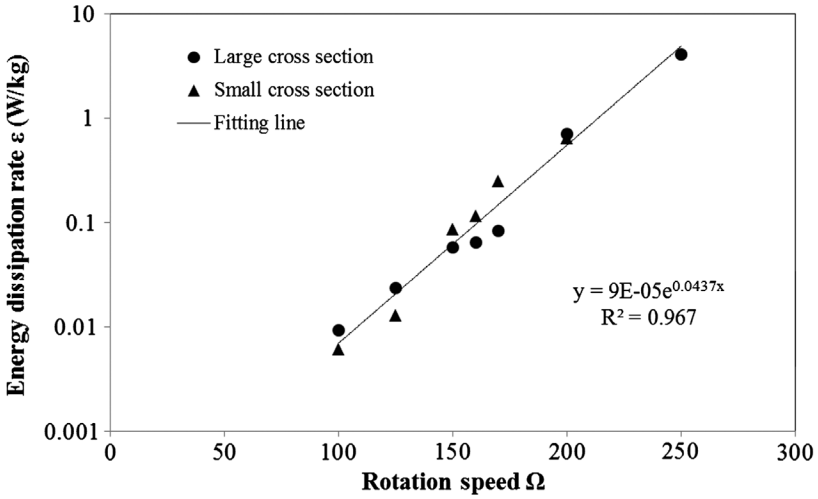

Figure. 3.1.2: Energy dissipation rate based on the rotation speed of the Baffled Flask obtained by the Boufadel group (Zhao et al. 2015).

For baffled flask experiments, we used Alaska North Slope (ANS) as fresh and shade-weathered for approximately 15% mass loss. It is an oil commonly tested in the USA. The EPA BFT conditions was pursued first which requires a rotation speed of 200 RPM with a DOR of 1:20. In addition to the conditions of the EPA BFT, we used oil without dispersant, and we conducted experiments at a rotation speed of 250 RPM and a DOR of 0.0 (no dispersant) and 1:50 and 1:25. The goal is to provide a basis for uncertainty in the laboratory and/or in the field. The energy dissipation rate for the 200 RPM and 250 RPM is needed as input to the model VDROP, and it was obtained from Figure 3.1.2. which was developed based on measurements in the Baffled Flask in a prior work by the Boufadel group (Zhao et al., 2015).

Table 3.1.1 summarizes the experimental conditions used in the baffled flask experiments to obtain the oil droplet size distributions (DSDs) after 10 minutes of mixing. The experiments were conducted using both fresh and weathered ANS crude oil under different dispersant-to-oil ratios (DORs) and mixing intensities. Two parameters, K_b and b, were kept constant at 3 and 0.12, respectively, for all cases. Here, K_b represents the breakage coefficient (Eq. A2), which controls the rate at which larger oil droplets are broken into smaller droplets under turbulent conditions. A larger K_b corresponds to a greater tendency or rate of droplet breakup. The parameter "b", Eq. A2, accounts for the resistance of the oil phase to deformation and breakup due to its viscous properties. Thus, b represents the effect of oil viscosity on the breakup process. We dedicated an effort to keep K_b and b constant across experiments even if the match was not particularly good in some cases.

Table 3.1.1: Experiments conducted in the Baffled Flask to obtain the oil droplet size distribution. The mixing duration was 10 minutes. For the DOR of 0.0, droplets larger than 60 microns were removed from the observed data; for the simulated 10 minutes were allowed to evolve prior to computing the DSD.

	State	DOR	RPM/eps (Watt/kg)	D50(um) Obs/Sim	K_b	b	Jo(kg/s)
C1	Fresh ANS	0.0	200/1.0	13.86/18.90	3	0.12	0

C2	Weathered ANS	0.0	200/1.0	15.36/18.91	3	0.12	0
C3	Fresh ANS	1:25	200/1.0	2.74/2.73	3	0.12	5e-11
C4	Weathered ANS	1:25	200/1.0	3.52/3.17	3	0.12	5e-11
C5	Weathered ANS	0.0	250/4.0	17.94/18.92	3	0.12	0
C6	Weathered ANS	1:50	250/4.0	8.28/7.54	3	0.12	5e-11
C7	Weathered ANS	1:20	250/4.0	2.73/3.10	3	0.12	5e-10

Prior to the experiments, the oil density, viscosity, and oil–water interfacial tension (IFT) were measured. The measured properties are summarized in Table **Error! Reference source not found.**.

Table 3.1.2: Oil properties of fresh and weathered Alaska North Slope (ANS) and Hibernia oils at 25 °C, including dispersant-treated cases at different dispersant-to-oil ratios (DORs)

Oil type	**Density; kg/m^3**	**Viscosity; cP**	**Interfacial tension; mN/m**
Baffled Flask			
Fresh ANS	881	15.8	6.89
15% Weathered ANS	923	155.4	8.03
15% Weathered ANS, DOR 1:50	923	155.4	0.0023
15% Weathered ANS, DOR 1:25	923	155.4	0.0011
15% Weathered ANS, DOR 1:20	923	155.4	0.0005
Ohmsett			
Fresh Hibernia	859.1	21.2	17.6
5% Weathered Hibernia	867.7	29.7	20.9
20% Weathered Hibernia	890.1	86.1	24.6

Table 3.1.2 shows that 15% weathering of ANS increased the oil viscosity by approximately an order of magnitude, while the oil–water interfacial tension (IFT) increased by about 17%. For Hibernia oil, 5% weathering increased the viscosity from 21.2 to 29.7 cP and the IFT from 17.6 to 20.9 mN/m. Dispersant application substantially reduced the IFT. For weathered ANS oil, the IFT decreased from 8.03 mN/m without dispersant to 0.0023 mN/m at a dispersant-to-oil ratio (DOR) of 1:50, while further increasing the DOR from 1:25 to 1:20 resulted in only a small decrease in IFT, from 0.0011 to 0.0005 mN/m.

Figures 3.1.3 and 3.1.4 show the oil DSD obtained using the LISST100X for the experiments reported in Table 3.1.1. Figure 3.1.3 illustrates the oil droplet size distributions (DSDs) measured after mixing at 200 RPM for 10 minutes, followed by a 10-minute static period, for both fresh and weathered ANS oil at DOR = 0 and 1:25. The results show a clear difference between the untreated and dispersant-treated cases. In the absence of dispersant, the DSDs extend over a relatively broad range of droplet sizes, with a substantial fraction of the measured volume associated with droplets larger than several tens of micrometers. In contrast, the addition of dispersant shifts the distribution strongly toward the smaller size range, with most of the measured volume concentrated in droplets of only a few micrometers. This difference demonstrates the strong effect of dispersant addition on the resulting DSD and provides valuable datasets to train the VDROP model. The y-axis scales differ between the panels because the volume fractions are substantially larger in the dispersant-treated cases at the smallest droplet sizes.

Figure 3.1.4 presents the corresponding DSD measurements for weathered ANS oil mixed at 250 RPM for 10 minutes, followed by a 10-minute static period, at DOR = 0, 1:50, and 1:20. These results further demonstrate the effect of dispersant concentration on the droplet population. The untreated case (DOR = 0) exhibits a broad distribution extending into the larger droplet-size range, whereas the dispersant-treated cases show a pronounced concentration of the volume fraction within the few-micrometer range. The comparison between DOR = 1:50 and DOR = 1:20 also shows that increasing the dispersant-to-oil ratio primarily affects the magnitude and distribution of the fine-droplet fraction, while the overall response remains dominated by small droplets. As in Figure 3.1.3, the expanded y-axis range is necessary to display clearly the magnitude and shape of the fine-droplet distributions.

For the DOR=0 cases, one notes the presence of droplets larger than 60 microns. There is no physical justification for them to be submerged considering their rise velocity, the static period of 10 minutes, and the short distance for them to travel (3.0 cm). We hypothesized that these relatively large droplets were primarily the result of coalescence during the static period and subsequent sampling and therefore should not be considered representative of the submerged DSD. To test our hypothesis, we assumed initial droplet concentrations of 100 mg/m3 for different sizes and we evaluated numerically the concentration after 10 minutes of no-mixing. We also assumed the turbulent diffusion coefficient to be around 10^{-7} m^2/s. This value is larger than the molecular diffusion coefficient (10^{-9} m^2/s) but was selected to account for slight vibrations of the flask that could induce weak residual motion during the 10-minute no-mixing period.

Figure. 3.2.5 presents the predicted concentration profiles after 10 minutes for oil droplets with a density of 880 kg/m^3 and diameters ranging from 1 to 50 μm. At time zero, all sizes were at 100 mg/m3 (a vertical line). The results show a strong dependence of concentration on the droplet size. Droplets of size 1–10 μm remained nearly uniformly distributed throughout the water column, indicating that buoyancy is insufficient to cause significant resurfacing within the measurement period. By contrast, larger droplets rapidly migrated toward the surface. For the 30 μm droplets, approximately 90% of the oil concentration accumulated near the surface after 10 minutes, while only a small fraction remained suspended. Droplets larger than 30 μm exhibited even stronger resurfacing tendencies and are effectively removed from the sampled water column. These results suggest that a droplet diameter of approximately 30 μm represents a practical cutoff size for the baffled flask test, with smaller droplets remaining dispersed and larger droplets largely resurfacing before the concentration measurements are performed. We concluded therefore that droplets larger than 60 microns are most likely the result of coalescence in the tubing of the pumps and/or in the LISST instrument.

For the cases with dispersant, one notes the presence of droplets in the 7 to 12 microns, but the largest volume fraction is around 2.0 microns. We believe that the small sizes are due to tip-streaming consistent with our prior investigations, as discussed below.

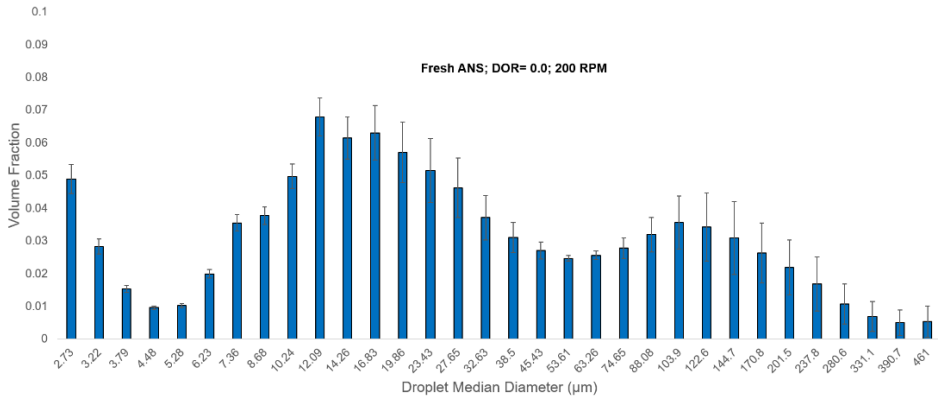
Fresh ANS; DOR= 0.0; 200 RPM
Volume Fraction
0.1
0.09
0.08
0.07
0.06
0.05
0.04
0.03
0.02
0.01
0
2.73 3.22 3.79 4.48 5.28 6.23 7.36 8.68 10.24 12.09 14.26 16.83 19.86 23.43 27.65 32.63 38.5 45.43 53.61 63.26 74.65 88.08 103.9 122.6 144.7 170.8 201.5 237.8 280.6 331.1 390.7 461
Droplet Median Diameter (µm)

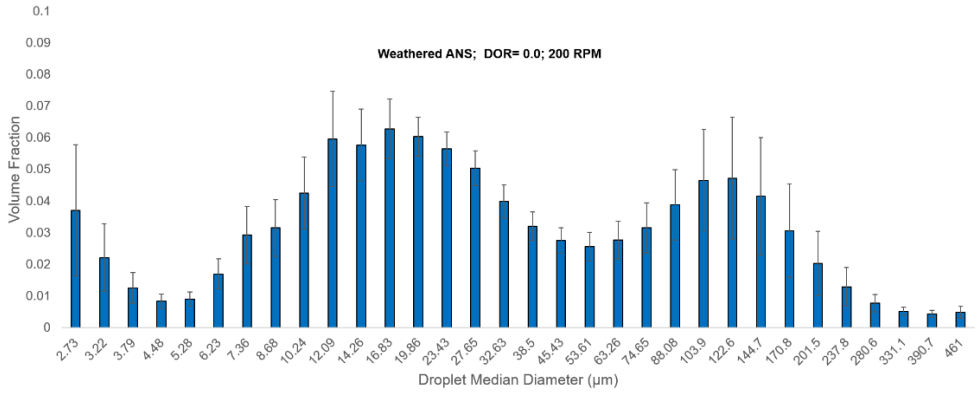
Weathered ANS; DOR= 0.0; 200 RPM
Volume Fraction
0.1
0.09
0.08
0.07
0.06
0.05
0.04
0.03
0.02
0.01
0
2.73 3.22 3.79 4.48 5.28 6.23 7.36 8.68 10.24 12.09 14.26 16.83 19.86 23.43 27.65 32.63 38.5 45.43 53.61 63.26 74.65 88.08 103.9 122.6 144.7 170.8 201.5 237.8 280.6 331.1 390.7 461
Droplet Median Diameter (µm)

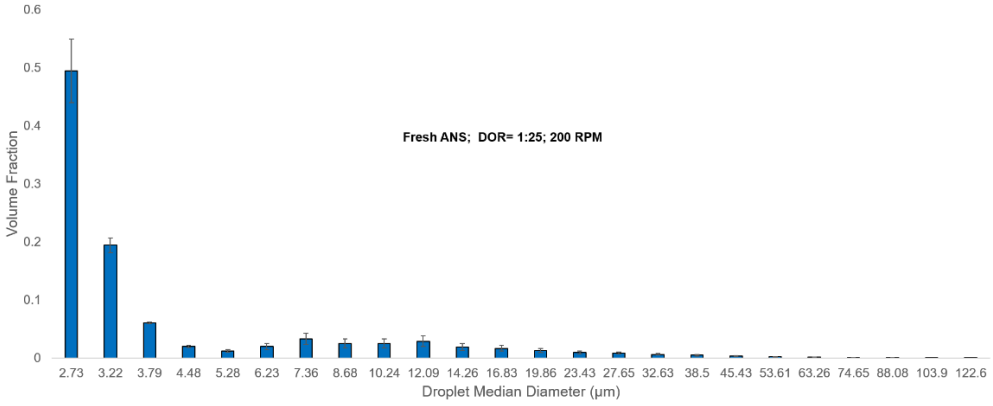
Fresh ANS; DOR= 1:25; 200 RPM
Volume Fraction
0.6
0.5
0.4
0.3
0.2
0.1
0
2.73 3.22 3.79 4.48 5.28 6.23 7.36 8.68 10.24 12.09 14.26 16.83 19.86 23.43 27.65 32.63 38.5 45.43 53.61 63.26 74.65 88.08 103.9 122.6
Droplet Median Diameter (µm)

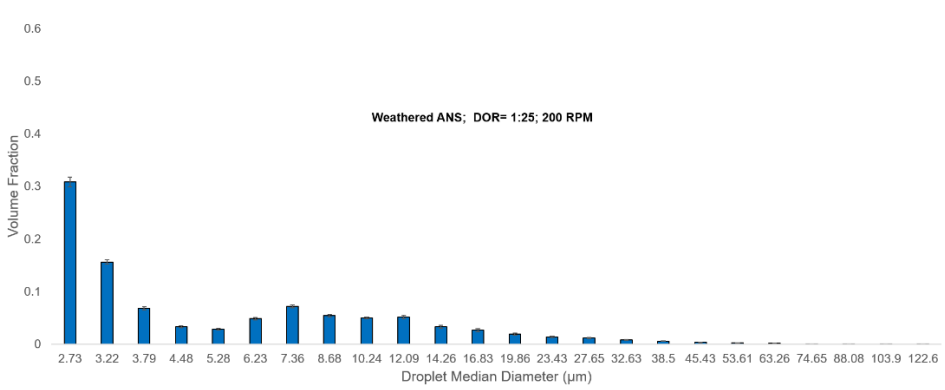

Figure. 3.1.3: Incremental oil droplet size distribution measured by LISST after mixing at 200 RPM in the Baffled Flask for 10 minutes, and 10 minutes after stoppage of the mixing. Fresh and weathered Alaska North Slope were considered at DOR of 0.0 (no dispersant) and 1:25. Note the large vertical scale and smaller droplet scale for the cases with dispersant.

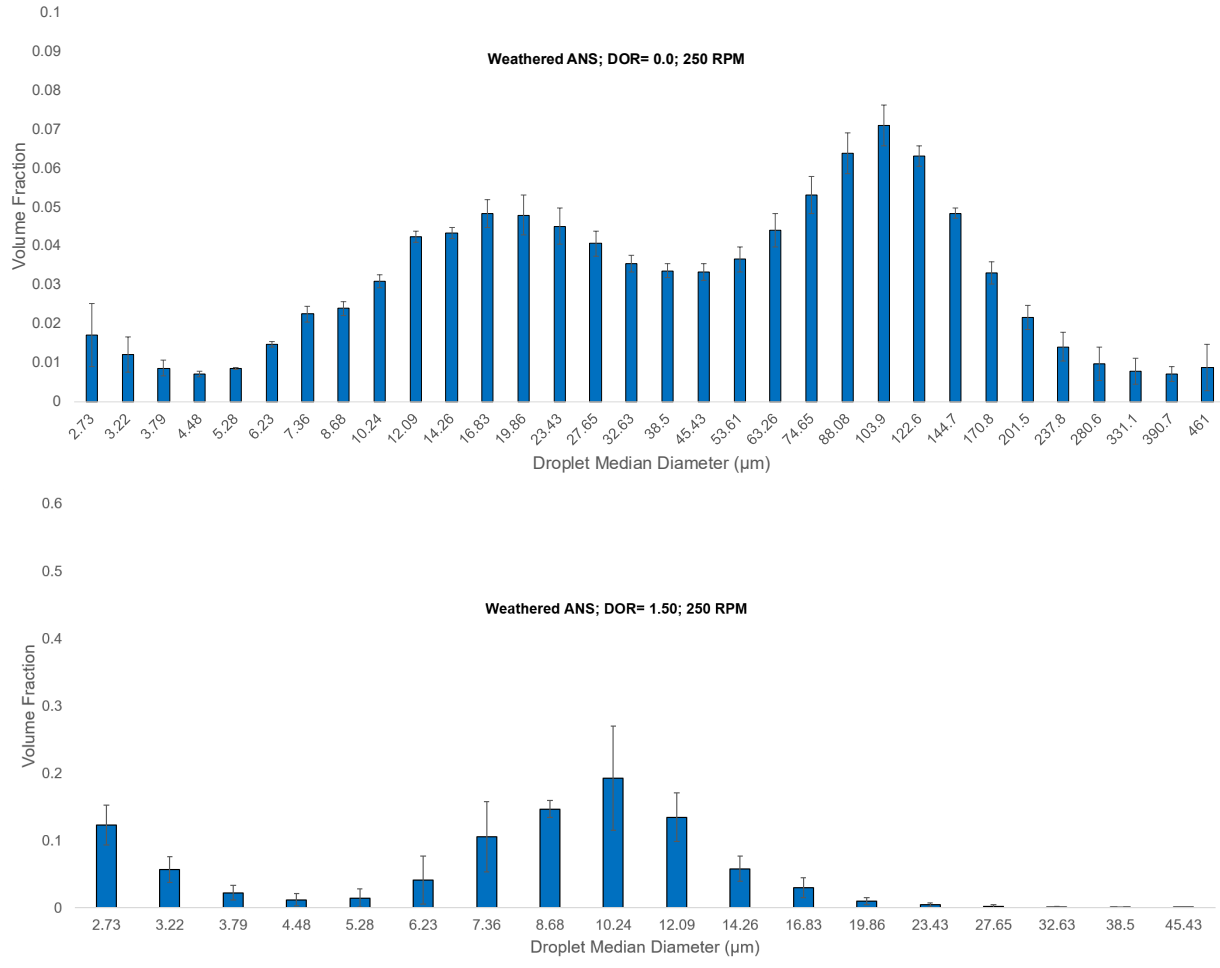

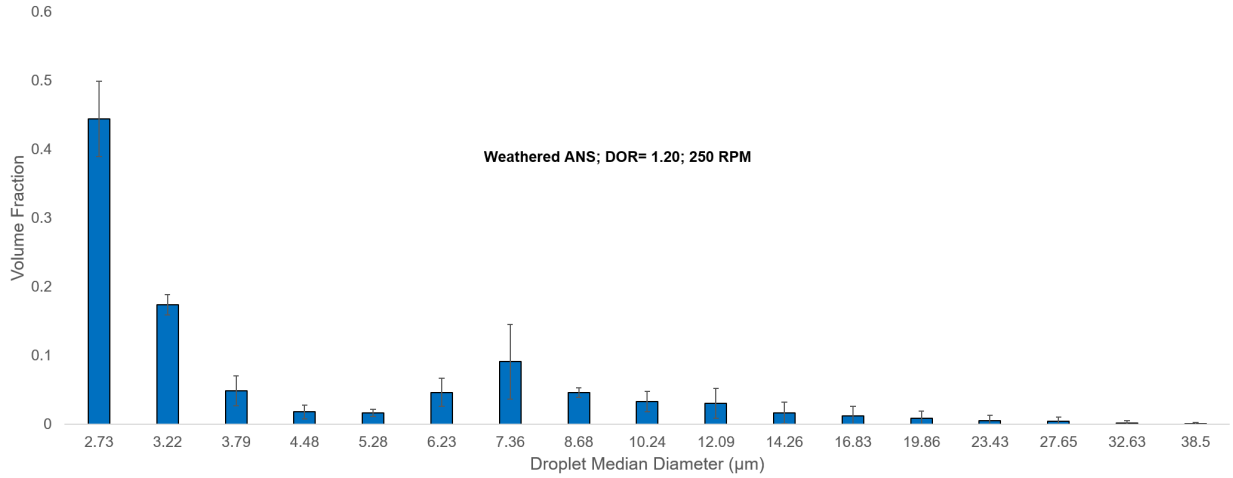

Figure. 3.1.4: Incremental oil droplet size distribution measured by LISST after mixing at 250 RPM in the Baffled Flask for 10 minutes, and 10 minutes after stoppage of the mixing. Weathered Alaska North Slope were considered at DOR of 0.0 (no dispersant), 1:50, and 1:20. Note the large vertical scale and smaller droplet scale for the cases with dispersant.

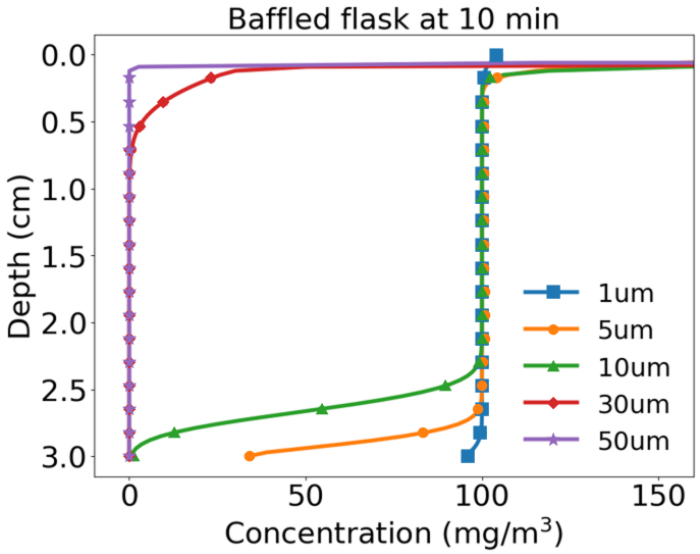

Figure. 3.2.5: Concentration of droplets of different sizes in the baffled flasks at various depths 10 minutes after stoppage of mixing. The initial value for each droplet size was assumed to be 100 mg/m^3 for simplicity. The 50 microns are completely resting at the water surface. Thus, LISST measurements providing values larger than 60 microns (for example) are most likely due to coalescence within the apparatus for sampling.

3.2 Numerical Modeling of Dispersed Oil Droplet Size Distribution

The evolution of oil droplet size distributions can be described using a population balance model, where the DSD evolves through two competing mechanisms that are breakup and coalescence (Figure. 3.2.3a); large oil droplets may fragment into smaller droplets when subjected to sufficiently strong turbulent stresses, while smaller droplets may collide and merge to form larger droplets. Consequently, the resulting droplet size distribution (DSD) is governed by the dynamic balance between these two processes. This was captured in the model VDROP developed by the Boufadel group (Zhao et al., 2014). In fairly general conditions during oil spills in natural systems, the oil holdup (i.e., the oil volume as a fraction of the total volume of oil and water) is smaller than 30% which makes coalescence negligible (as the chance of oil encountering oil is small). Thus, oil breakup becomes the only mechanism affecting DSD evolution. An oil holdup larger than 30% exists in the riser of oil reservoir, near the orifice in case of a blowout, and at a calm water surface.

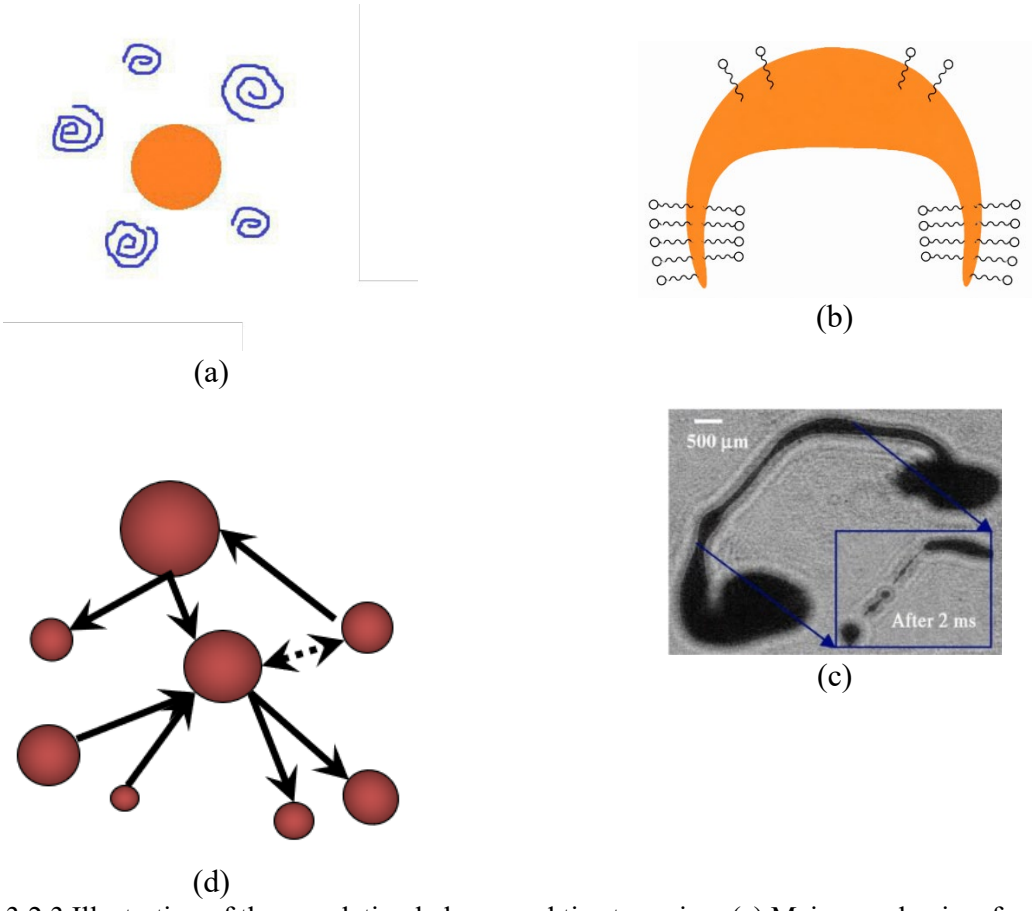

Figure. 3.2.3 Illustration of the population balance and tip streaming. (a) Major mechanism for oil droplet breakup at low dispersant dosage; turbulent eddies collide with droplets and break them. (b) Schematic illustration of the effect of dispersants on the morphology of oil droplets; the tails of the surfactant is hydrophobic and thus embed within oil. (c) Experimental observation of tip streaming, showing the formation of a thread of fine oil droplets resulting from the reduced oil–water interfacial

tension (IFT) (Gopalan and Katz 2010). (d) Illustration that the VDROP model accounts for both breakup and coalescence of droplets dynamically.

The model VDROP has been successfully applied to investigate oil droplet breakup, coalescence, and transport processes in both laboratory-scale and field-scale oil spill scenarios. The model can accurately predict the temporal evolution of droplet size distributions by accounting for turbulent energy dissipation, droplet collision frequencies, and coalescence efficiencies (Cui et al. 2020b; Zhao et al. 2014a). Important parameters in it are the breakage coefficient, K_b, Eq. A2 the viscous resistance parameter "b", Eq. A7 and the tip streaming parameter J_o (discussed next).

For most medium to light oils the interfacial tension (IFT) between oil and water is the major stabilizing force of the droplet by comparison to oil viscosity. However, when dispersant is added the IFT decreases, and the resistance force due to oil viscosity becomes important. This is actually the reason behind the "V" in VDROP, i.e., to capture the resistance force due to oil viscosity. An empirical parameter appears in the viscous force, labelled "b" (Eq. A7), and it took the value of 0.06 when working with high viscosity oils. However, as we are working with medium to low viscosity oils, we elected to re-estimate "b" based on the data.

When dispersant is present at a high concentration, tip streaming occurs. It is the "sloughing off" of oil from the droplet through filaments (Fig. 3.2.1.b) due to a substantial reduction in the oil–water interfacial tension (IFT) by the dispersant. Under low-IFT conditions, elongated oil droplets can develop thin fluid threads at their tips (Figure. 3.2.3c), which subsequently break into numerous micron-sized droplets (Gopalan and Katz 2010; Li et al. 2017). These droplets can contribute substantially to the fine-droplet fraction and may significantly alter the overall droplet size distribution. The Boufadel group amended VDROP in 2017 to add a tip streaming module (Zhao et al. 2017b). The new formulation accounts for the mass transfer from parent droplets to micron-sized droplets generated through tip-streaming processes. By explicitly representing this additional breakup pathway, the modified model was able to capture the enhanced production of small droplets (i.e., under 10 microns) observed in the experimental results of Zhao et al. (2017b). The goal of the present work is to further test that module on additional experimental results.

The release of oil mass due to tip streaming can be calculated as:

$$\frac{dM_i(d_i,t)}{dt} = -k_{tip} J_0 \tag{3.2.1}$$

Where M_i is the mass of droplets of size d_i, $k_{tip} = \frac{\Delta\sigma}{\sigma_0}\frac{\mu_c}{\mu_c+\mu_d}\mathrm{Re}_d^{1/2}\left(\frac{\nu_c}{D}\right)^{1/3}$ is a dimensionless coefficient, $\Delta\sigma$ is the maximum attainable IFT reduction relative to the IFT σ_0 of clean interface, μ_c and μ_d are the viscosity of continuous phase (water) and dispersed phase (oil), Re is the Reynolds number of the droplet, ν_c is the kinetic viscosity of the continuous phase (water), and D is the molecular diffusion coefficient in the continuous phase. The term J_o is a mass flow rate

estimated to be 10^{-12} kg/s by Zhao et al. (2017a) by fitting to data. It is further estimated in this work.

A direct comparison between VDROP and the results above could occur if one took samples immediately after stoppage of mixing. However, in the EPA BFT, one is required to wait 10 minutes after mixing stoppage to sample from the bottom of the flask. During these 10 minutes droplets will rise due to their buoyancy, which depends on the oil density and their size (Stokes Law). This means that droplets that reach the surface within 10 minutes will not be sampled.

To simulate this, we assumed a uniform spatial arrangement of droplets across the 3.0 cm depth of the BF, and we allowed the droplets to rise to the surface within 10 minutes of a hydrostatic regime in the BF whose water depth is 3.0 cm. Thus, we simulated the BF mixing by assuming mixing at a given energy dissipation rate for 10 minutes which generated the DSD, and then we assumed that the droplets rise to the surface due to buoyancy. As the physics of the rise velocity is well determined, the approach allows calibration of VDROP. Recall that the results in Figure. 3.2.5 show that droplets that are 50 microns or larger will reach the surface within 10 minutes. This indicates that droplets larger than 60 microns that could be measured in the LISST instrument are most likely due to coalescence in the tubing. Fortunately, when scaling the EPA BFT (i.e., with dispersant at 1:20), the formed droplets are much smaller than 60 microns (see Figure 3.1.4), and thus modeling their rise is not necessary. In this project, we conducted experiments without dispersant for a scientific purpose, but such is not required by the EPA BFT.

For the initial droplet diameter to use in VDROP (i.e., at the beginning of the mixing duration), two configurations were considered: a single maximum initial droplet diameter and a linear droplet size distribution. Because the initial DSD represents the droplet population immediately prior to entrainment into the water column, we hypothesize that the intense shear generated by wave breaking within the upper millimeter of the water column produces a non-uniform, triangular-shaped distribution. The triangular distribution is particularly attractive because it requires minimal additional assumptions and therefore introduces the least subjectivity into the model formulation.

The results of the fitting are reported in Figure 3.2.2 and Figure 3.2.3, where one notes that VDROP was able to capture the overall trends of the observed DSDs. Our goal was not to match exactly the observations but to reproduce within certain accuracy (say 20% of each value) the general behavior of the system. It is important to note that simplified approaches use only the d50 for comparison and assume an oil DSD such as a lognormal. In our case, we produced the full DSD, and we computed the d_{50} subsequently. Table 3.1.1 shows that our d_{50} is very close to the observed one for all cases, with a difference of less than 10% in most cases. It is also important to appreciate that the tip-streaming module helps capture the substantial production of small droplets in cases with dispersant, thereby improving the model's ability to reproduce the enhanced fine-droplet fraction observed in the experimental DSDs.

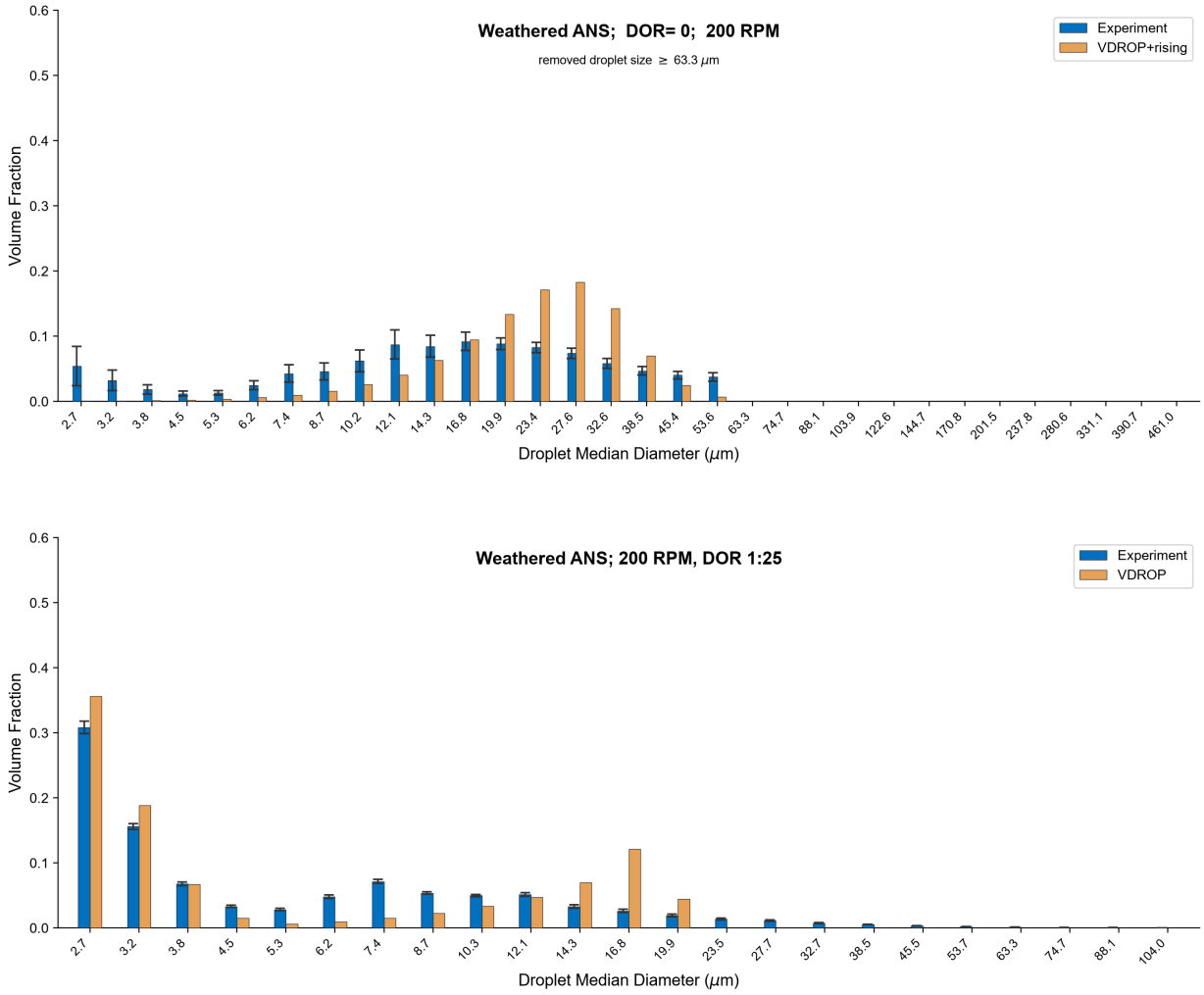

Figure. 3.2.2: Incremental oil droplet size distribution measured by LISST and predicted by VDROP simulations after mixing at 200 RPM in the Baffled Flask for 10 minutes. Weathered Alaska North Slope oil was considered at DOR of 0.0 (no dispersant) and 1:25. Note the larger vertical scale and smaller droplet size range for the dispersant case.

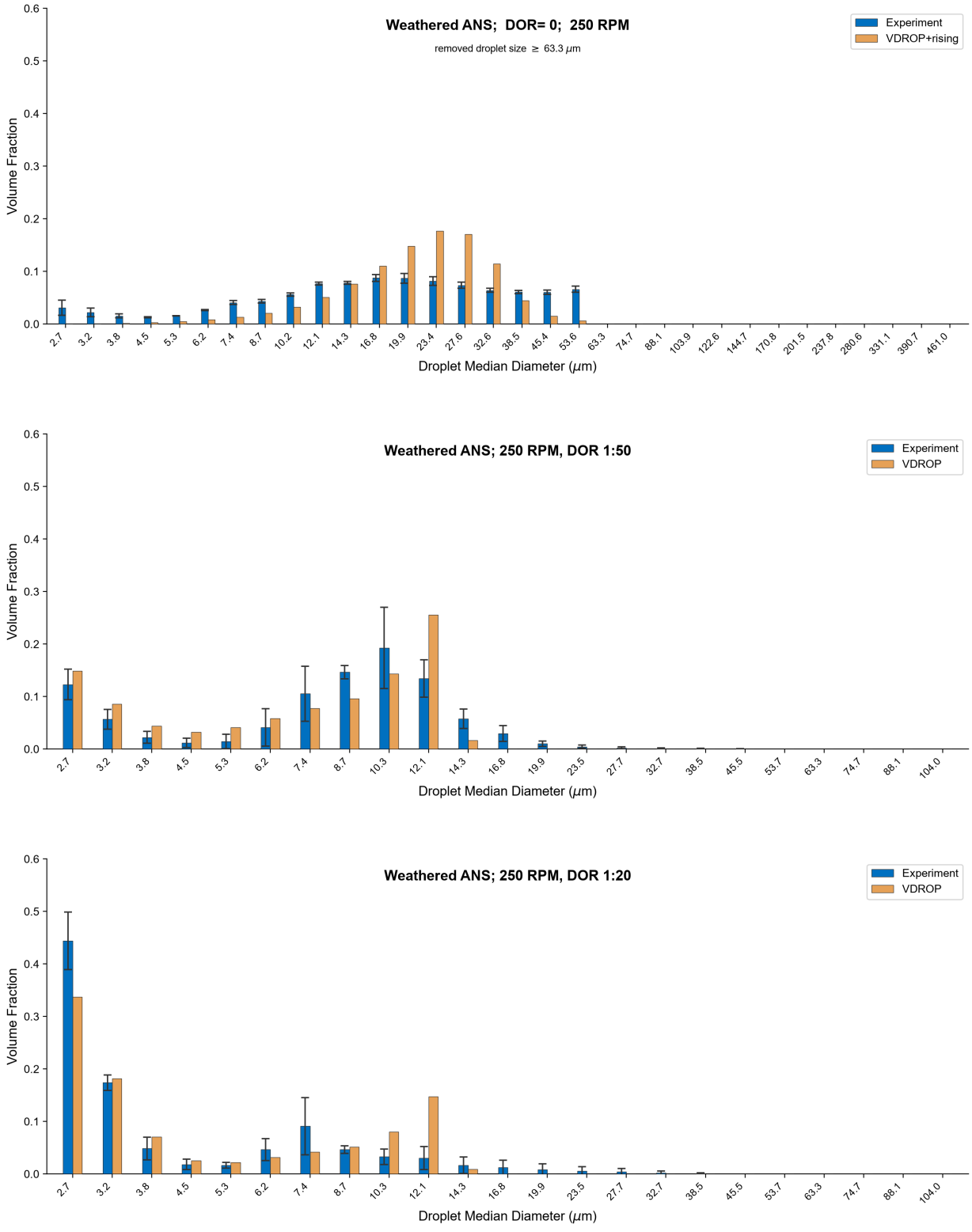

Figure. 3.2.3: Incremental oil droplet size distribution measured by LISST and predicted by VDROP simulations after mixing at 250 RPM in the Baffled Flask for 10 minutes, and 10 minutes after stoppage of the mixing. Weathered Alaska North Slope were considered at DOR of 0.0 (no

dispersant), 1:50, and 1:20. Note the large vertical scale and smaller droplet scale for the cases with dispersant.

4 Large-scale Wave Tank

4.1 Experiments

Large-scale wave tank experiments have been reported in Liu et al. (2026). The goal herein is to closely analyze the resulting data and to estimate the parameters of the VDROP model needed to scale up the results.

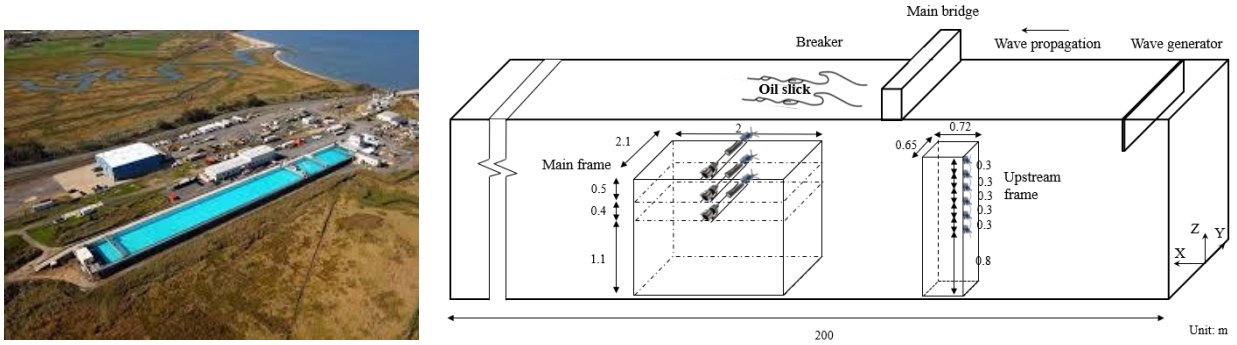

(a) (b)

Figure. 4.1.4 Bird's eye view of the OHMSETT Wave Tank and Experimental Setup
The left figure (a) shows the birds eye view of the Ohmsett wave tank (203 x 20 x 2.4 m), and the figure on the right (b) shows the configuration of the upstream and downstream frames, along with the location of the bridge.

The experiment was conducted at Ohmsett (National Oil Spill Response Research and Renewable Energy Test Facility, Leonardo, New Jersey, USA) in a large outdoor wave tank measuring 203 m in length, 20 m in width, and 2.4 m in water depth (Figure. 4.1.4(a)). The facility is equipped with a wave generator located at the southern end of the tank.

Breaking waves were generated using the frequency-sweep technique developed by Boufadel et al. (2017). Two wave trains with different wave periods were produced sequentially and propagated toward each other, resulting in a plunging breaker approximately 100 m from the wavemaker. Prior to wave generation, a surface slick containing 20 L of weathered Hibernia crude oil was released at the anticipated breaker location. The oil was initially confined within a floating square frame measuring 0.9 m × 0.9 m. Based on the released oil volume and the frame area, the initial slick thickness was estimated to be approximately 2.5 cm. After removal of the confinement frame, the oil-covered area expanded by approximately four to six times before wave impact, reducing the average oil thickness to a few millimeters (approximately 5 mm).

It should be noted that the oil used in the Ohmsett experiments was different from the oil types used in the BFT experiments. Therefore, the DSDs measured in the two experimental systems may

exhibit differences due to the different physical and chemical properties of the oils. However, the scale-up analysis does not rely on a direct one-to-one comparison of the absolute DSD between the Ohmsett and BFT experiments. Instead, it focuses on the overall behavior and evolution of the DSD during the post-formation stage and its response to the relevant mixing conditions. By focusing on these general characteristics, the scale-up analysis minimizes the influence of oil-specific differences and provides a basis for evaluating the applicability of the relationship across the two experimental scales.

For dispersant-treated cases, dispersant was applied at a dispersant-to-oil ratio (DOR) of 1:20. This ratio is a rule-of-thumb value recommended by the National Academies of Sciences, Engineering, and Medicine (2019). Following dispersant application, the oil was allowed to interact with the dispersant for at least 60 s before the confinement frame was removed. In all experiments, the breaking wave reached the oil slick approximately 15–20 s after removal of the frame.

Flow velocities were measured using Vector Acoustic Doppler Velocimeters (ADV; Nortek, Rud, Norway) mounted on two frames: an upstream frame and a downstream (main) frame (Figure. 4.1.4b). The incident wave height immediately prior to breaking was approximately 0.6 m and its height was measured using an ultrasound wave gauge located adjacent to the upstream ADV system. Measurements obtained approximately 15 m upstream of the breaking location were used to characterize the evolution of the incoming breaker.

Oil droplets generated by wave breaking were measured using instruments mounted on the main frame (Figure. 4.1.4b). The frame measured 2.0 m × 2.1 m × 2.0 m (L × W × H) and consisted of three sampling elevations: Level A (1.9 m above the tank bottom), Level B (1.5 m), and Level C (1.1 m). Note that the water level in the tank was 2.4 m. Oil droplet size distributions were measured using shadowgraph cameras (Belmar Inc., Miami, Florida, USA) and a Laser In-Situ Scattering and Transmissometry instrument (LISST-100X; Sequoia Scientific Inc., Bellevue, Washington, USA). The shadowgraph cameras measured droplets ranging from approximately 100 μm to 4 cm, with an image resolution corresponding to a pixel size of 13.3 μm. This size range is representative of oil droplets generated in untreated oil dispersions. The LISST-100X measures droplet diameters from 2 μm to 461 μm, which corresponds to the size range typically observed following effective dispersant application. As discussed by Zhao et al. (2018), droplets smaller than the lower detection limit may contribute to apparent increases in measured concentrations near 1–2 μm.

Potential interference from air bubbles in LISST measurements was neglected in the present study. Owing to the substantially larger density difference between air and water than between oil and water, entrained bubbles are expected to rise rapidly and dissipate before accumulating at the measurement depths (approximately 0.9 m and 1.4 m below the water surface). Furthermore, bubble concentrations are expected to decrease significantly during the later stages of the entrainment process, several minutes after wave breaking. For untreated oil cases, the influence of bubbles was further minimized because larger bubbles could be identified in shadowgraph images and excluded from analysis.

An underwater camera (IPC608UW, LinoVision USA, Texas, USA) was mounted on the main frame to record the evolution and transport of the dispersed oil plume.

Figure. 4.1.5 shows selected times of the breaking waves on oil slicks. The top two images (Figure. 4.1.5a and b) show whitecap formation and subsequent oil dispersion of the slicks due to wave action. The lower images (Figure. 4.1.5c, d, e and f) captured the plumes from an underwater perspective. Figure. 4.1.5a, c and e present untreated oil, where individual droplets ranged in size from hundreds of microns to centimeters and are visible. By contrast, Figure. 4.1.5b, d and f show oil treated with a 1:20 dispersant-to-oil ratio (DOR), resulting in micron-scale droplets forming in caffe-latte type of a cloud plume, where individual droplets are not visible. Figure. 4.1.5 g and h show the ShadowGraph images for the untreated and treated oils (with dispersant), respectively. For untreated oils, the oils slick was broken into droplets in the hundreds of micrometers range; while for oil with dispersant, the droplets at the micron-scale formed a miscible flow with the water.

The results of these experiments will be presented later along with modeling results of water level, water speed, and oil plume and droplets.

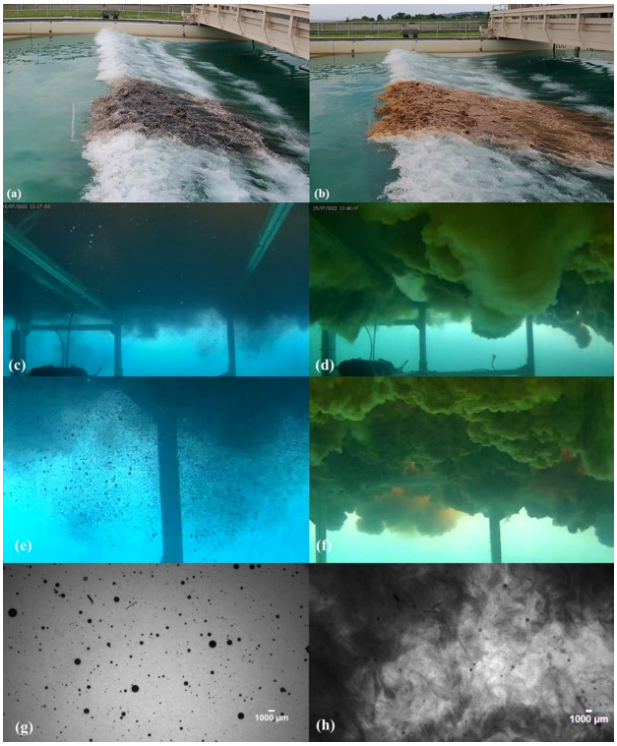

Figure. 4.1.5: Images of the Ohmsett oil experiments. (a) Top view of 5% shade-weathered Hibernia oil without dispersant; (b) Top view of 5% shade-weathered Hibernia oil with dispersant (at DOR 1:20); (c) underwater view of untreated oil; (d) underwater view of oil treated with dispersant; (e) close-up underwater view of untreated oil; (f) close-up underwater view of oil treated with dispersant; (g) ShadowGraph image of untreated oil forming droplets in the hundreds-of-micrometers size range; (h) ShadowGraph image of dispersed oil, where micron-scale droplets are not resolved by the camera and form a miscible-like flow with the surrounding water

4.2 High-fidelity computational fluid dynamics (CFD) simulations

Computational Fluid Dynamics (CFD) has been widely used to simulate wave hydrodynamics and estimate key parameters governing oil dispersion, such as eddy diffusivity and turbulent energy dissipation rates. In this project, Large Eddy Simulation (LES), which explicitly resolves large-scale turbulent structures, was employed to reproduce experiments conducted at the Ohmsett facility. The filtered Navier–Stokes equations were solved to simulate the wave dynamics and resolve the large-scale turbulent eddies generated by breaking waves. The Smagorinsky–Lilly subgrid-scale (SGS) turbulence model was employed to represent unresolved turbulent motions. The Volume of Fluid (VOF) method was used to capture the air–water interface, while oil was assumed to be a "passive scalar" (i.e., it moves due to wave flow but does not impact water flow). Its transport was simulated using advection-diffusion equations. The governing equations used in the LES simulations are provided in Appendix B.

Due to computational limitations, it was not feasible to simulate the entire wave tank (approximately 200 m in length and 20 m in width). Instead, upstream water-level measurements were used as boundary conditions to reproduce the hydrodynamic conditions in the downstream wave-breaking region. The computational domain measured 36 m (length) × 1.2 m (width) × 2.4 m (depth) and was discretized into approximately 17 million computational cells. The width of 1.2 m was selected to allow for some flow in the transverse direction.

Because the computational grid resolution is on the order of several millimeters, the model cannot explicitly resolve the breakup of oil droplets into micron-sized or even submillimeter droplets. To address this issue, the LES simulations were coupled with the VDROP model, which predicts the oil droplet size distribution (DSD) in each cell at each time step given the DSD at the previous time step. The coupling is performed within each of the approximately 17 million CFD cells at time intervals of approximately 0.1 s. All governing equations, turbulence closures, and the VDROP model were solved using a modified version of the interFoam solver from the open-source CFD platform OpenFOAM. The simulations were executed on the Wulver High-Performance Computing (HPC) cluster using two compute nodes (128 CPU cores in total) to efficiently resolve the wave-breaking and oil-dispersion processes.

The VDROP model requires calibration of the droplet breakup parameter, (K_b), to match experimental observations. After experimentation with many values, two values of (K_b) (2.0 and 10.0) were considered as a suitable range for Kb as each value gave a reasonable agreement at a given location or within a given duration.

Figure. 4.2.6 demonstrates good agreement between the simulated and measured water surface elevations. The numerical model successfully reproduces both the magnitude and timing of the wave peaks and troughs throughout the record. In particular, the arrival times of the major wave crests are well captured, indicating that the wave generation and propagation processes are accurately represented in the simulation. Although the overall agreement is satisfactory, the simulated wave crests appear slightly more compact and steeper than those observed experimentally. This discrepancy may be attributed to limitations in grid resolution, numerical diffusion, or uncertainties associated with the experimental measurements.

Several factors may contribute to the observed deviations. First, the Ohmsett wavemaker possesses substantial mechanical inertia and therefore cannot reproduce the prescribed electronic input signal perfectly. Second, the large tank width (20 m) allows the development of transverse currents and three-dimensional flow structures that are not fully represented in the numerical model. Third, wave breaking is an inherently nonlinear process, and small disturbances in the flow field can amplify rapidly as the breaker evolves. Such localized fluctuations are difficult to reproduce exactly, particularly using an engineering-scale CFD model designed to capture the dominant hydrodynamic features rather than every instantaneous detail of the flow. Overall, the close agreement between the simulated and measured velocity fields indicates that the model successfully reproduces the velocity fields associated with wave breaking.

Of particular importance is the crest responsible for initiating the breaking event at approximately t = 52 s. The simulation accurately captures both the timing and amplitude of this wave crest, providing confidence that the numerical model reproduces the key hydrodynamic conditions (i.e., eddy diffusivity and energy dissipation rate) leading to wave breaking. Since oil entrainment and droplet breakup are strongly controlled by the local turbulence and flow structures generated during the breaking process, accurately reproducing the breaker initiation is essential for subsequent simulations of oil transport and droplet size evolution. The close agreement between the simulated and measured water levels therefore supports the use of the numerical model for investigating the oil entrainment processes associated with plunging breakers.

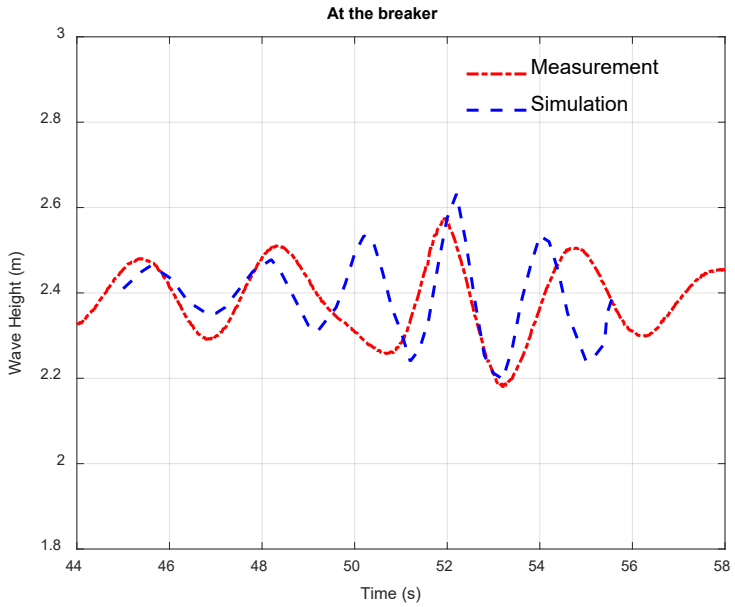

Figure. 4.2.6: Simulated and measured water level at the downstream frame (see Figure. 4.1.4). The simulation was able to capture closely the largest wave, but not the smaller ones, which is probably due to imperfection in the tank and nonlinearity of waves produced 100 m upstream.

Figure. 4.2.7 demonstrates good agreement between the simulated and measured horizontal (along-tank) and vertical velocity components. The numerical model successfully reproduces the major velocity fluctuations observed during the experiment, particularly those associated with the

breaking event. Both the horizontal and vertical velocity components reach magnitudes of approximately 0.4 m s^{-1} near t = 70 s, and the pronounced velocity variations occurring between t = 64 and 72 s are captured well by the simulation. A minor discrepancy is observed between t = 60 and 62 s; however, this difference is relatively small and is not expected to significantly influence the interpretation of oil entrainment and droplet breakup processes.

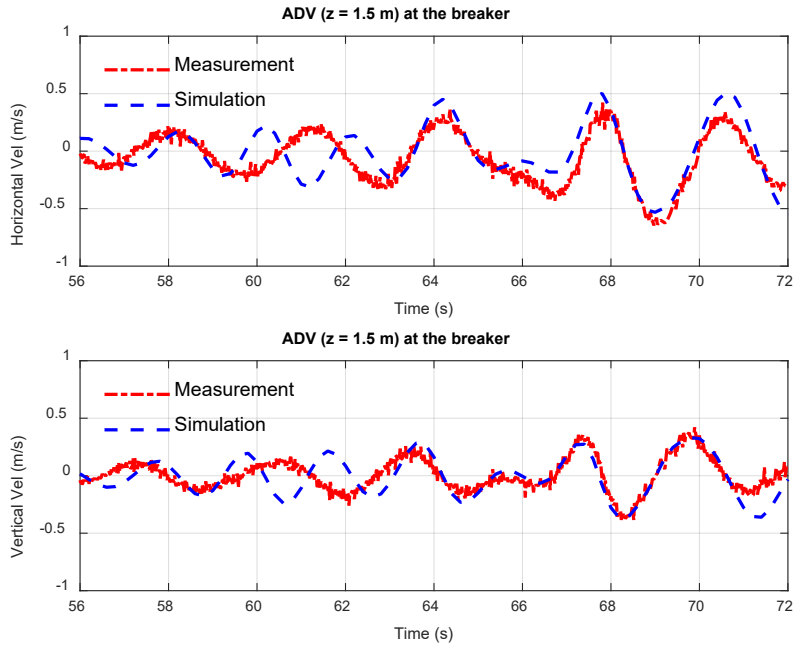

Figure 4.2.7: Simulated and measured velocity times series at the elevation of 1.5 m (i.e., 0.9 m below the static water level at the Ohmsett tank).

Contours of the energy dissipation rate are reported in Figure 4.2.3, and one notes that maximum values were near the surface, and they approached 0.1 watt/kg, which is comparable to the energy dissipation rates measured for breaking waves under ocean conditions. Wickley-Olsen et al. (2007, AMOP) measured maximum value of 0.5 watt/kg in the Bedford Institute of Oceanography (BIO) tank for a 0.4 m breaker. Miller, Katz et al. measured an energy dissipation rate of 0.01 watt/kg for their 0.3 m breaker, and Cui et al. (2020a) measured 0.4 watt/kg for the breaker in the BIO tank. This indicates that the modelled results are within the measured range. Following the initial plunging event, the residual breaker continues to propagate downstream and produces localized regions of elevated dissipation rate at the wave front (Figure. 4.2.8c). These residual turbulent structures contribute to sustained mixing and turbulence generation in the wake of the breaking event. As the wave train propagates away from the breaking region and the flow calms, the turbulent kinetic energy dissipation rate gradually decreases (Figure. 4.2.8d). This behavior is associated with the intense turbulent energy dissipation within the breaking zone, where large droplets may undergo breakup and generate smaller droplets that are subsequently advected by the flow. Following the passage of the wave train, most of the 1500 μm droplets remain within approximately 0.5 m below the free surface over the 20–25 m region. In contrast, the 150 μm droplets penetrate deeper into the water column and spread over a larger downstream area. These results highlight the strong influence of droplet size on oil entrainment, transport, and vertical distribution under breaking-wave conditions.

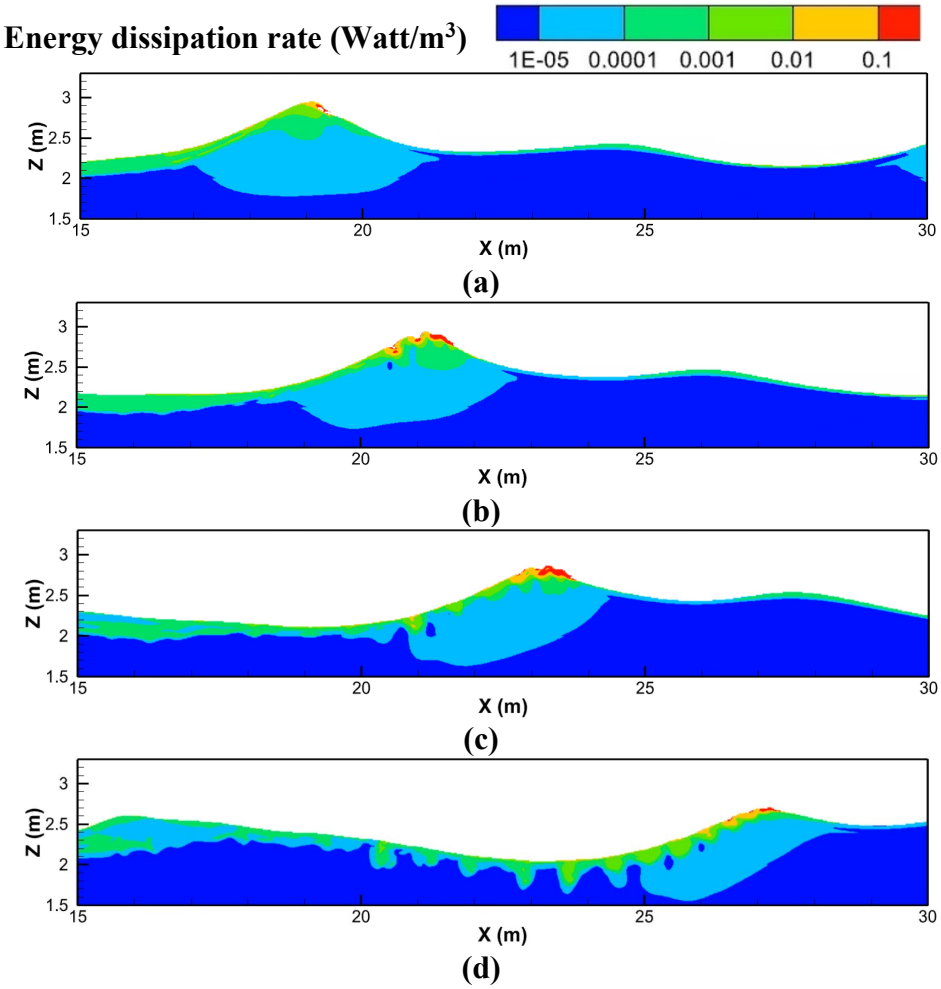

Figure. 4.2.8: Simulated energy dissipation rate. The evolution of the spanwise-averaged energy dissipation rate during wave breaking: (a) t = 22.2 s, (b) t = 22.8 s, (c) t = 23.4 s, and (d) t = 24.6 s. Note that the maximum value is comparable to that in the baffled flask of 1.0 watt/kg.

Figure. 4.2.9 compares the simulated and observed oil plume contours, where the dashed line represents the iso-contour of the spanwise-averaged oil concentration. During the initial stage of wave breaking, the simulated oil plume penetrates slightly deeper into the water column than observed experimentally (Figure. 4.2.9a). However, during the active breaking phase and the subsequent wave propagation period (Figures 4.2.9b–4.2.9d), the simulated plume agrees well with the observations in both shape and extent. Overall, the 0.01 kg m^{-3} concentration contour effectively captures the outer boundary of the oil plume. Oil concentrations increase rapidly toward the water surface, consistent with trends observed in both laboratory experiments and field observations. These results indicate that the CFD model successfully reproduces the major features of oil entrainment and plume evolution under breaking-wave conditions.

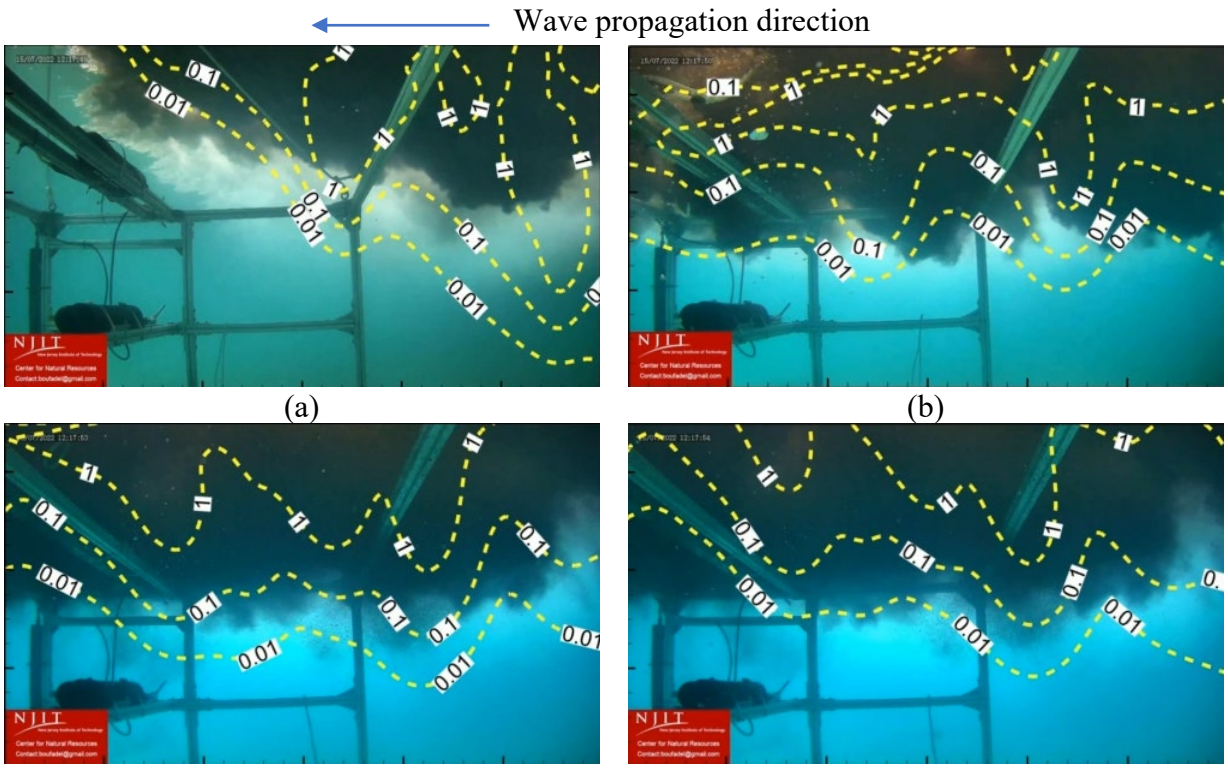

Figure. 4.2.9: Oil plumes observed and simulated (using CFD). The dashed lines indicate the concentration of oil in kg/m^3.

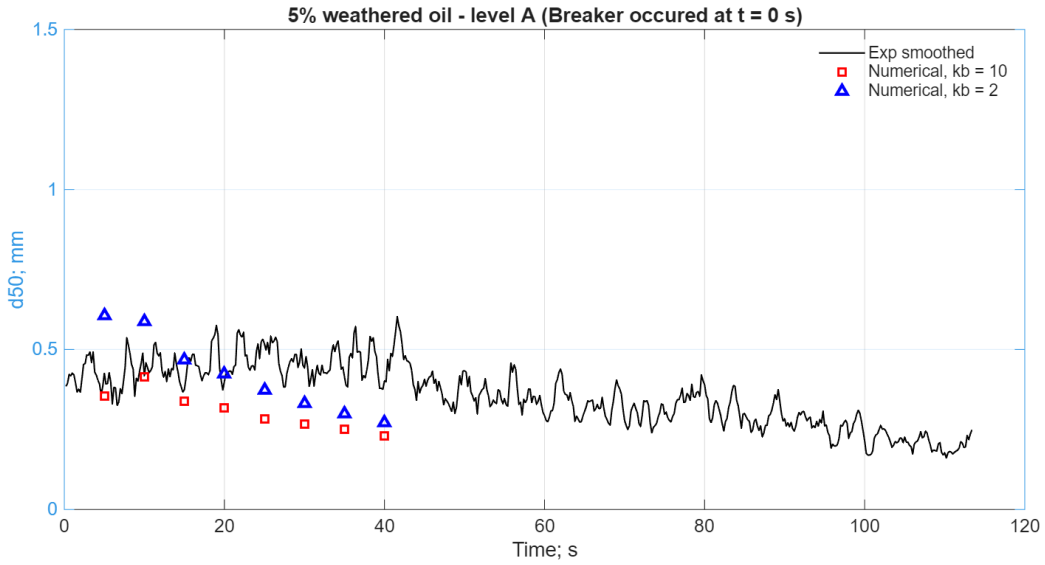

(a)

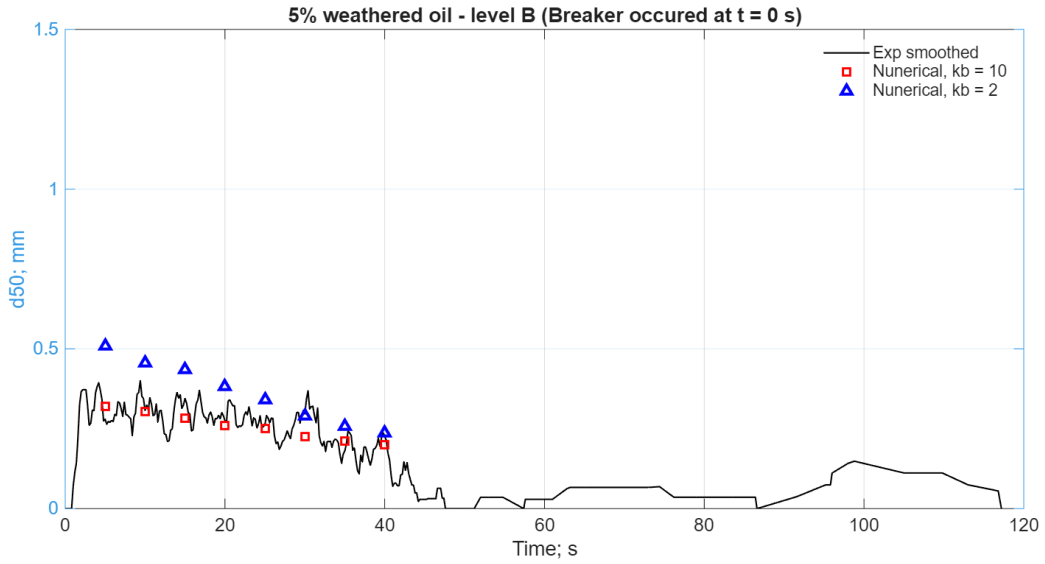

(b)

Figure. 4.2.10: Measured and simulated d_{50} at two sample locations at x = 24 m within two elevations: (a) 1.9 ~ 2.1 m, and (b) 2.1 ~ 2.3 m. Two different K_b values were considered: 2 and 10.

Figure. 4.2.10b shows that, at the lower sampling location, the simulated d_{50} agrees well with the experimental observations. In contrast, the case with $K_b = 2$ overestimates d_{50}, particularly during the first 10 – 15 s following wave breaking. Overall, Figure. 4.2.5 demonstrates that the proposed model performs well in predicting the d_{50} under breaking wave conditions. The measured d_{50} of all experiments at various locations are reported in Table 4.2.1, and one notes that for the case without dispersant, the simulated results of Figure 4.2.5 are comparable to the experimental data.

Table 4.2.1: Ohmsett experiments with a breaker using Hibernia oil. Still water level (i.e., water level without waves) was 2.4 m. "Saturated" means that the LISST could not read due to high concentrations. NA= Not available (large uncertainty in these results)						
#	Oil amount	Oil type	Dispersant	d_{50} Level A 0.5 m depth	d_{50} Level B 0.9 m depth	d_{50} Level C 1.3 m depth
1	20L	5% weathered	no	432 µm	306 µm	NA
2	20L	20% shade-weathered	no	645 µm	398 µm	NA
3	20L	20% photo-oxidized	no	726 µm	400 µm	NA
4	20L	5% weathered	DOR=1:20	Saturated	5.3 µm	3.2 µm
5	20L	20% weathered	DOR=1:20	Saturated	9.2 µm	5.5 µm
6	20L	20% photo-oxidized	DOR=1:20	Saturated	9.6 µm	4.6 µm

5 Modeling of oil droplets dispersion in the upper ocean

The dispersion of oil droplets at sea is the result of three mechanisms: Formation of droplets due to the action of waves, diffusion in the water column due to hydrodynamics, and rise of individual droplets due to buoyancy. The action of diffusion and buoyancy on the concentration of droplets of size "d", c_d, is captured by the vertical advection-diffusion equation:

$$\frac{\partial c_d}{\partial t} = K(z)\frac{\partial^2 c_d}{\partial z^2} - w_d \frac{\partial c_d}{\partial z} \tag{5.1}$$

where w_d is the terminal rise velocity of droplets of size d, and K(z) is the eddy diffusivity (or diffusion coefficient) given by:

$$K(z) = \left(\frac{\kappa u_*}{\phi}\theta\right)(z + z_o)\left(1 - \frac{z}{MLD}\right)^2 \tag{5.2}$$

where *MLD* denotes the mixed layer depth, u_* is the friction velocity, and κ is the Von Karman constant; the term θ and ϕ are enhancement factor and stability function, respectively. Z_o is the approximate surface roughness. Common values are 0.1 m and 0.5 m. Figure. 5.1 illustrates a representative vertical distribution of eddy viscosity for a mixed layer depth (MLD) of 30 m and

a depth-averaged eddy diffusivity of 10^{-3} m^2/s. This value is considered reasonable because the mean eddy diffusivity below the MLD has been reported to be on the order of 10^{-4} m^2/s Large et al. (1994). The eddy diffusivity increases with depth from the surface, reaches a maximum at approximately one third of the MLD (10 m herein), and then gradually decreases to zero at the base of the mixed layer (z = 30 m herein).

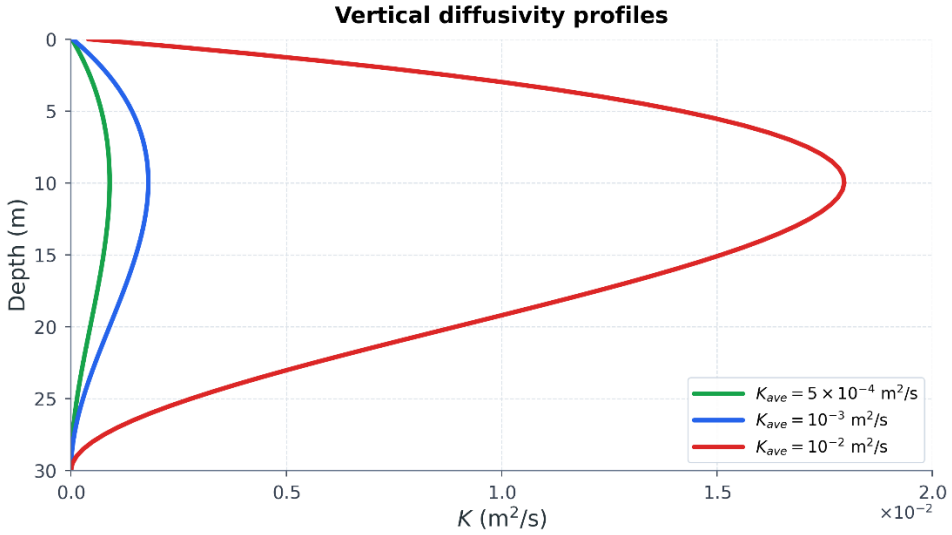

Figure. 5.11: Eddy diffusivity profile for a mixed layer depth (MLD) of 30 m. Below the MLD, the eddy diffusivity is around 10^{-4} m^2/s.

Using the eddy diffusivity profile for $K_{ave}=10^{-3}$ m^2/s in Figure. 5.11, numerical simulations were conducted for individual oil droplets with a density of 880 kg/m^3 released within the water column. In these simulations, only two physical mechanisms were considered: turbulent diffusion, represented by the prescribed eddy diffusivity profile, and droplet buoyancy, which drives upward migration toward the water surface. No droplet breakup, coalescence, or interactions between droplets were included, as this analysis focused on the vertical transport of oil droplets during post-formation stage. The vertical position of the droplet plume centroid was then calculated as a function of time, and the results are presented in Figure. 6.13.

Figure. 6.13 illustrates the competing effects of turbulent diffusion and buoyancy on oil droplets of different diameters. The 10, 30, and 50 µm droplets exhibited similar behavior, with their plume centroids remaining several meters below the surface throughout the 6-hour simulation. This is unlike the case of the BF, and is due to the large diffusion herein. By contrast, the 100 µm droplets remain concentrated near the surface, indicating that buoyancy is sufficiently strong to overcome turbulent transport and rapidly return the droplets to the water surface.

The results therefore reveal a clear separation between two droplet populations. Droplets with diameters of 50 µm and smaller behave as dispersed droplets, whereas 100 µm droplets tend to resurface and remain near the surface. This transition is consistent with the commonly adopted rule of thumb that droplets smaller than approximately 70 µm can be considered effectively

dispersed. The error bars represent the vertical spreading of the droplet plume due to turbulent diffusion and demonstrate that, despite substantial vertical spreading, droplet size remains the primary factor controlling oil residence time within the water column.

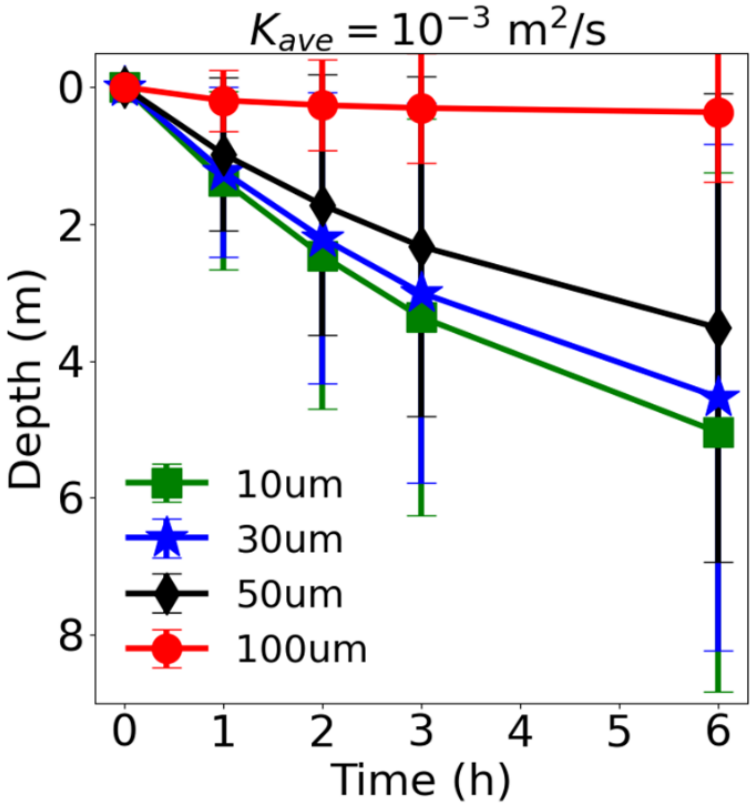

Figure 5.2: Centroid of plumes of various droplet sizes as function of depth and time. The error bars represent one standard deviation.

6 Procedure for scaling-up

We argue in this work that there is no simple way to scale up such as using a linear statistical correlation, and that the main factor for scaling up is by comparing the submerged oil droplet size distribution (DSD) at a comparable stage of post-entrainment evolution. In the EPA BFT, the prescribed procedure is to sample the water 10 minutes after mixing is stopped. During this period, buoyancy causes larger droplets to rise toward the surface, such that the measured DSD reflects both droplet formation during mixing and subsequent droplet rise.

We did not establish a fixed temporal cutoff for the Ohmsett experiments. Instead, we allowed the oil plume to continue evolving beyond the breaking event, which occurred over a period of a minute, as droplets were subsequently transported and redistributed by turbulent mixing and buoyancy.

Therefore, rather than imposing a universal cutoff time, the present study considers the evolution of the DSD following the breaking event. Future research should investigate whether a standardized post-breaking observation time or observation window can be established for wave tank experiments. Measurements of DSD and submerged oil fraction at multiple times after breaking could be used to identify a representative observation period based on the rate of DSD evolution and vertical oil transport. Such a criterion could provide a more consistent basis for comparing wave tank results with BFT measurements and, ultimately, with field-scale dispersant effectiveness.

For a given oil at a given state of weathering, there are four factors that impact the oil DSD. They are: 1) The IFT (as impacted by the DOR), 2) the energy dissipation rate, 3) the duration over which the energy dissipation rate occurs, and 4) the diffusion coefficient in the water body. Regarding the energy dissipation rate and its duration, one needs to measure not only the maximum value which occurs usually over a short duration but a representative value of that system. Alternatively, and based on our experience, one needs to accept a range for the energy dissipation rate. For example, a mean value of 0.4 watt/kg with a range from 0.1 to 1.0 watt/kg. Such a relaxation is based on the physics because turbulent systems are inherently nonlinear, and thus small disturbance could engender a large difference in velocities and local (in time and space) energy dissipation rates. The same argument applies to the diffusion coefficient in the mixed layer depth of the ocean, and coefficient whose value varies from 5.10^{-4} to 5.0×10^{-2} m^2/s and even larger. These coefficients not only vary because of turbulence but also because of natural variability in the forcing factors: wind, temperature, waves, etc.

The procedure is listed below and drawn in Figure 6.3:

1) Obtain the oil DSD from the BFT after 10 minutes of rest. Run VDROP+rise to match the DSD.
2) Assign three energy dissipation rate values at sea: The value from the BF, which is 1.0 watt/kg, and 0.3 watt/kg and 0.1 watt/kg.
3) Construct the curve of the IFT versus the DOR (see Figure 6.1), or use a curve for a similar oil/dispersant. Consider two DOR values: 1:20 and 1:50, the first represents the BFT and the second attempts to capture less than perfect contact between dispersant and oil.
4) Estimate the MLD at sea. It is a value that does not change much within a season. For open sea, adopt 30 m during the summer and 100 m during the winter. For closed water bodies, the MLD could be as small as 10 m. Regardless, this is a value that gets repeated on the average with seasons and thus should be available.
5) Run VDROP with these values until reaching steady state (one minute of VDROP).
6) Use the equation from Boufadel et al (2020) for the eddy diffusivity,

$$K(z) = \left(\frac{\kappa u_*}{\phi}\theta\right)(z+z_o)\left(1-\frac{z}{MLD}\right)^2 = A.(z+z_o)\left(1-\frac{z}{MLD}\right)^2 \qquad (6.1)$$

Thus, the average value over the depth MLD is given by:

$$K_{ave} = A.\left(\frac{MLD}{12}+\frac{z_0}{3}\right)^2 \qquad (6.2)$$

7) Select values K_{ave} value and compare to the graphs in Figure 6.2, which reports profiles of the droplets centroids with time for zo=0.1 m (the result does not change much with zo); three values of the eddy diffusivity, and three oil densities: 850; 900; and 950 kg/m3.
8) Interpolate between graphs to find the centroid of each size obtained from the BFT, and then weigh the centroid elevation by the volume fraction corresponding to each size. This would provide the centroid of the whole plume.

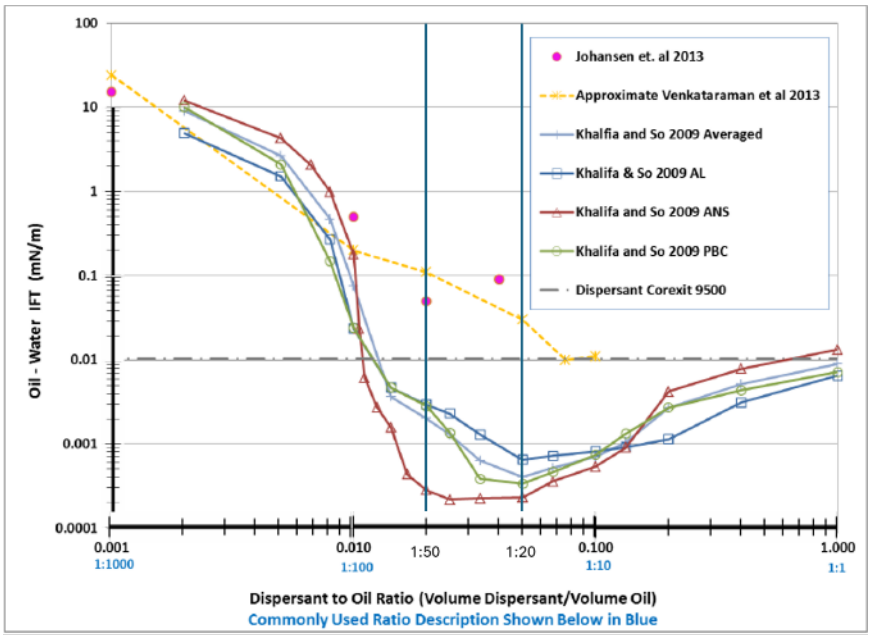

Crowley, Deborah, et al. "Modeling subsurface dispersant applications for response planning and preparation." International oil spill conference proceedings. Vol. 2014. No. 1. American Petroleum Institute, 2014.

Figure. 6.12: The interfacial tension (IFT) as function of dispersant to oil ratio (DOR).

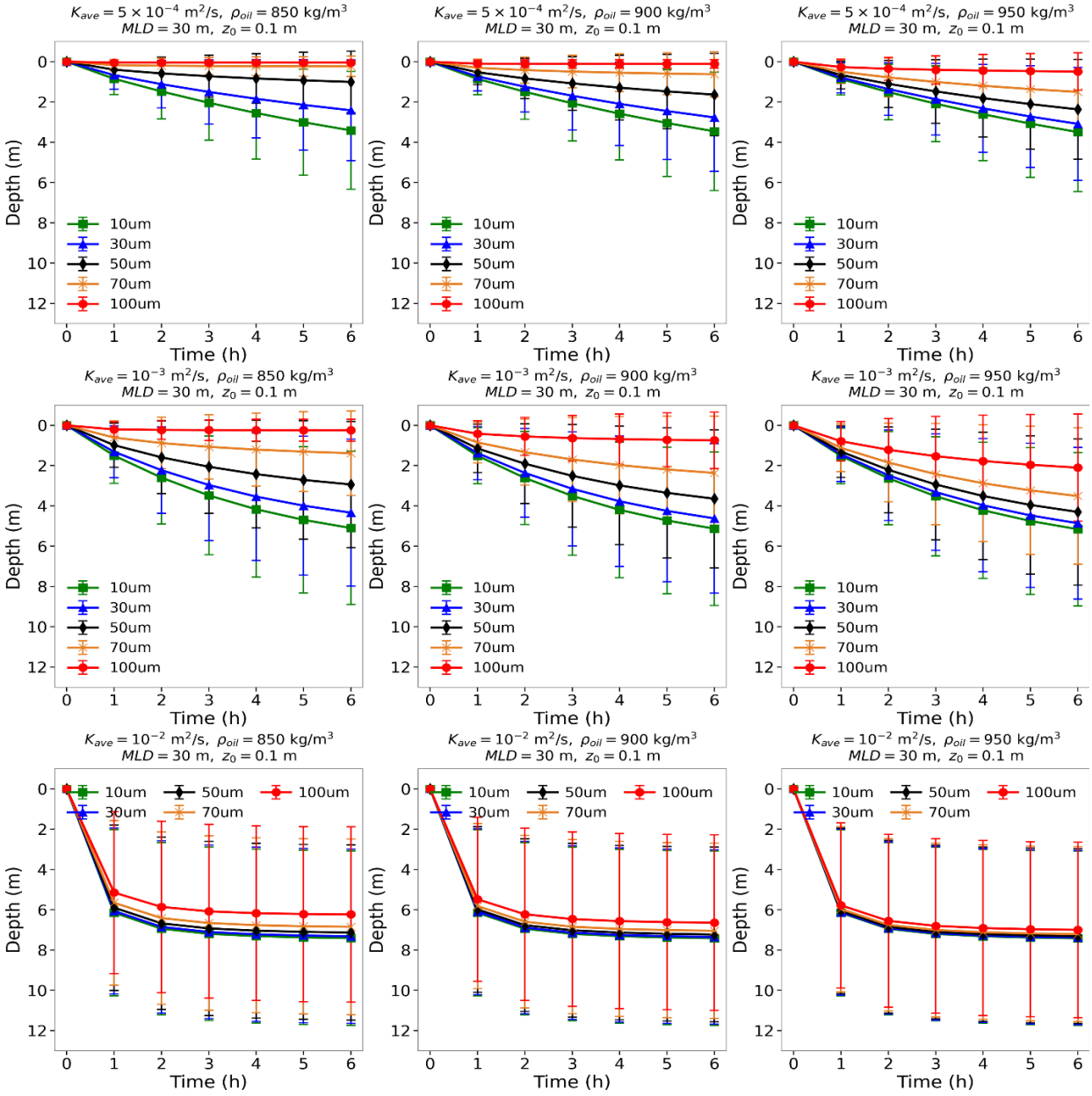

Figure. 6.13: Centroid of plumes of various droplet sizes as function of depth and time. Note that at the (arbitrary) time 2.0 hours, the centroid of droplets 50 microns or smaller is below the 1.0 m (arbitrary) mark. The error bars represent one standard deviation.

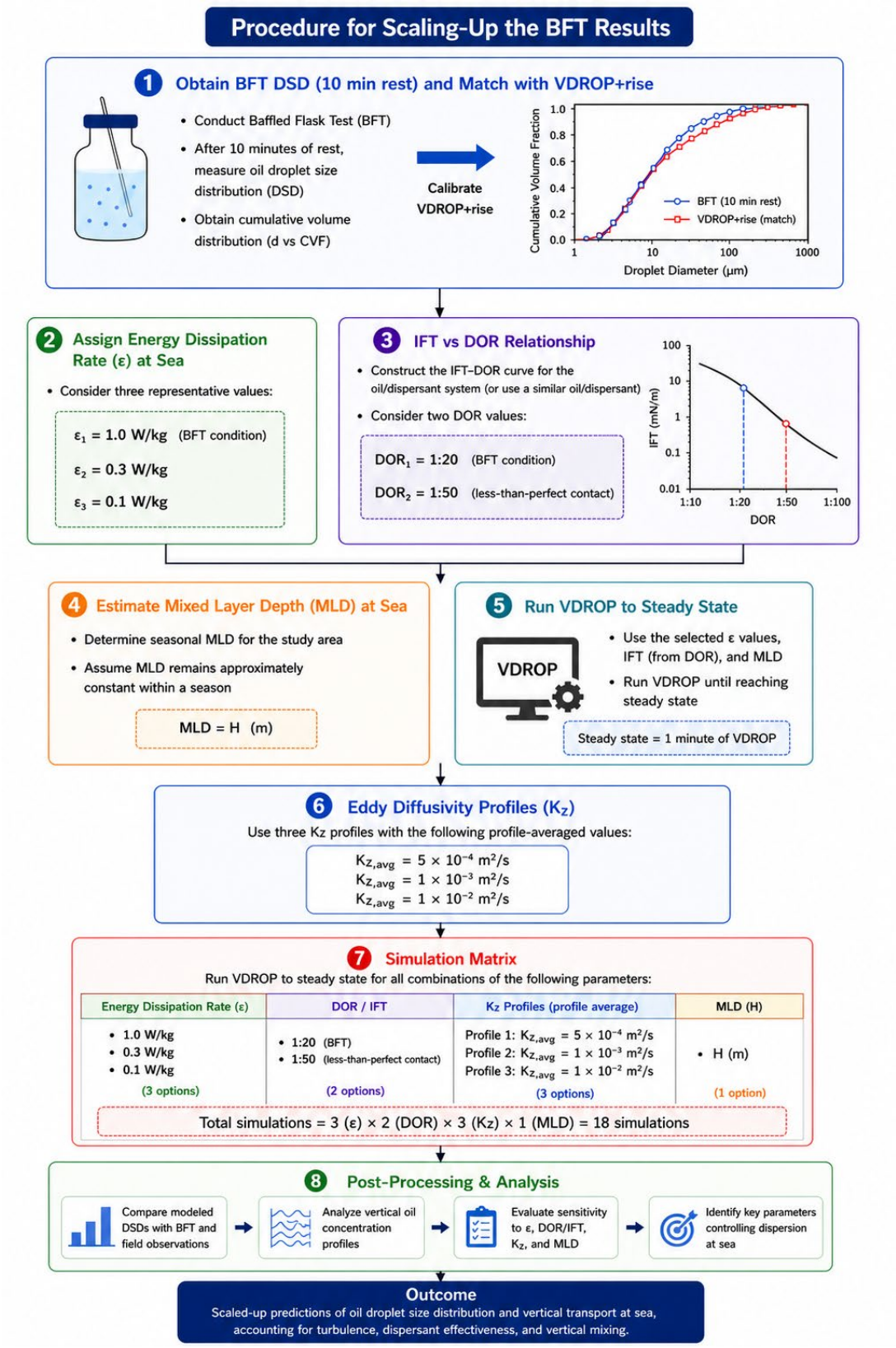

Figure 6.3: Scale up procedure diagram.

7 Conclusion

This study developed a physics-based framework for linking laboratory-scale dispersant effectiveness measurements with oil droplet formation, transport, and retention under breaking-wave in a wave tank and ocean conditions. The framework combined baffled flask experiments, Ohmsett breaking-wave experiments, large-eddy simulation (LES), the VDROP population balance model, and mixed-layer transport simulations. The principal findings are:

1. **Tip-streaming is an important mechanism for micron-sized droplet formation under low-IFT conditions.** The experimental observations showed substantial populations of droplets smaller than approximately 5–10 μm under dispersant-treated conditions. These droplets are consistent with tip-streaming, in which low IFT allows thin oil filaments to form and subsequently produce numerous fine droplets. Incorporating this mechanism into VDROP substantially improved prediction of the measured droplet size distributions.

2. **The LES–VDROP framework successfully reproduced key hydrodynamic and droplet-scale characteristics under breaking-waves.** The LES simulations reproduced the major features of the measured water-surface elevations, velocity fields, and vorticity distributions and provided estimates of turbulent energy dissipation and eddy diffusivity that are difficult to obtain from measurements alone. Coupling these hydrodynamic results with VDROP provided a physics-based approach for predicting droplet formation and evolution under breaking-wave conditions.

3. **Droplet size strongly controls the vertical transport and residence time of dispersed oil.** The mixed-layer simulations demonstrated clear competition between turbulent diffusion and buoyant rise. Smaller droplets remained suspended within the mixed layer for substantially longer periods, whereas larger droplets rapidly migrated toward the surface. In the simulations, droplets larger than approximately 200 μm resurfaced within minutes, while droplets of 50 μm and smaller were strongly influenced by turbulent diffusion.

4. **Droplet size distribution is therefore the key quantity for scaling dispersant effectiveness across different spatial and temporal scales.** The results indicate that scaling cannot be achieved reliably through a simple statistical conversion between laboratory and field measurements. Instead, the droplet size distribution should be predicted from the relevant IFT, dispersant-to-oil ratio, oil properties, turbulent energy dissipation, mixing duration, and turbulent diffusion characteristics of the system.

5. **Mixed-layer transport provides a practical framework for relating droplet size to field-scale dispersion effectiveness.** The simulations demonstrate that both the reference depth and observation time influence the apparent dispersant effectiveness. The results support the use of a reference depth on the order of **1 m** together with an observation period of approximately **2 hours** as a practical basis for evaluating whether dispersed oil remains sufficiently retained within the water column. These values should be regarded as practical reference conditions rather than universal thresholds, since the appropriate criterion may depend on the application and environmental conditions.

Overall, the study demonstrates that dispersant effectiveness is governed not only by the initial formation of small oil droplets, but also by their subsequent transport and retention in the water column. The integration of laboratory measurements, breaking-wave experiments, LES, VDROP, and mixed-layer transport modeling provides a physically based framework for translating dispersant performance across laboratory, wave-tank, and field-relevant scales. This framework can improve predictions of oil droplet size distributions, vertical oil transport, and dispersant effectiveness and thereby provide a stronger scientific basis for evaluating dispersant performance under realistic ocean conditions.

References

ASTM International. 2026. Standard test method for laboratory oil spill dispersant effectiveness using the baffled flask. West Conshohocken, PA: ASTM International.

Chemical characterization of the ohmsett tank water: Filtration and potential impact on dispersion effectiveness. 40th AMOP Technical Seminar on Environmental Contamination and Response; 2017.

Cui F, Geng X, Robinson B, King T, Lee K, Boufadel MC. 2020a. Oil droplet dispersion under a deep-water plunging breaker: Experimental measurement and numerical modeling. Journal of Marine Science and Engineering. 8(4):230.

Cui F, Zhao L, Daskiran C, King T, Lee K, Katz J, Boufadel MC. 2020b. Modeling oil dispersion under breaking waves. Part ii: coupling lagrangian particle tracking with population balance model. Environmental Fluid Mechanics. 20(6):1553-1578.

Gopalan B, Katz J. 2010. Turbulent shearing of crude oil mixed with dispersants generates long microthreads and microdroplets. Physical review letters. 104(5):054501.

Large WG, McWilliams JC, Doney SC. 1994. Oceanic vertical mixing: A review and a model with a nonlocal boundary layer parameterization. Reviews of Geophysics. 32(4):363-403.

Li C, Miller J, Wang J, Koley SS, Katz J. 2017. Size distribution and dispersion of droplets generated by impingement of breaking waves on oil slicks. Journal of Geophysical Research: Oceans. 122(10):7938-7957.

National Academies of Sciences E, Medicine, Division on E, Life S, Board on Environmental S, Toxicology, Ocean Studies B, Committee on the Evaluation of the Use of Chemical Dispersants in Oil Spill R. 2019. The use of dispersants in marine oil spill response. Washington (DC): National Academies Press (US)

Copyright 2019 by the National Academy of Sciences. All rights reserved.

Appendix c to part 300—requirements for product testing protocols and summary test data. 2024. U.S. Government Publishing Office; [accessed]. https://www.ecfr.gov/current/title-40/chapter-I/subchapter-J/part-300/appendix-Appendix%20C%20to%20Part%20300.

Zhao L, Boufadel MC, Conmy R, N, Wang B, Armanante P. 2015. Evaluation of mixing energy in the epa baffled flask using piv. Journal of Environmental Engineering, ASCE.

Zhao L, Boufadel MC, Socolofsky SA, Adams E, King T, Lee K. 2014a. Evolution of droplets in subsea oil and gas blowouts: Development and validation of the numerical model vdrop-j. Mar Pollut Bull. 83(1):58-69.

Zhao L, Gao F, Boufadel MC, King T, Robinson B, Conmy R, Lee K. 2017a. Oil jet with dispersant: Macro-scale hydrodynamics and tip streaming. AIChE Journal.

Zhao L, Gao F, Boufadel MC, King T, Robinson B, Lee K, Conmy R. 2017b. Oil jet with dispersant: Macro-scale hydrodynamics and tip streaming. AIChE Journal. 63(11):5222-5234.

Zhao L, Torlapati J, Boufadel MC, King T, Robinson B, Lee K. 2014b. Vdrop: A comprehensive model for droplet formation of oils and gases in liquids-incorporation of the interfacial tension and droplet viscosity. Chemical Engineering Journal. 253:93-106.

Appendixes

Appendix A: Equations of the VDROP model

The breakage probability $\beta(d_i, d_j)$ is computed by

$$\beta(d_i, d_j) = \frac{ef_{\min} + ef_{\max} - ef(d_i, d_j)}{\sum_{k=1}^{j-1}(ef_{\min} + ef_{\max} - ef(d_k, d_j))} \tag{A1}$$

Where $ef(d_i, d_j)$ is the formation energy from larger droplet d_j to smaller droplet d_i, $ef_{\max}$ and $ef_{\min}$ are the maximum and minimum formation energies associated with the generated surface.

The equation of breakage rate $g(d_j)$ is shown below:

$$g(d_j) = K_b \int_{n_e} S_{ed}({u_e}^2 + {u_d}^2)^{\frac{1}{2}} BE(d_j, d_e, \varepsilon, t) dn_e \tag{A2}$$

where K_b is a system-dependent parameter for droplet breakup and needs to be adjusted by the experimental data, dn_e is the eddy number per unit volume, and S_{ed} is the cross-section area of eddy. For a droplet d_i and an eddy with a diameter of d_e, S_{ed} can be computed by:

$$S_{ed} = \frac{\pi}{4}(d_e + d_i)^2 \tag{A3}$$

In the inertial subrange of the energy spectrum, the turbulent velocity of an eddy, u_e, and drop velocity u_d can be expressed as:

$$u_e = 2.27(\varepsilon d_e)^{1/3}; \quad u_d = 1.03(\varepsilon d_i)^{1/3} \tag{A4}$$

where ε is the total energy dissipation rate (watt/kg) computed based on the resolved velocity and the SGS eddy viscosity, ν_{sgs}, as follows:

$$\varepsilon = 2(\nu_m + \nu_{sgs})\bar{S} : \bar{S} \tag{A5}$$

where the meaning of ν_m and $\bar{S}$ can be found in Appendix B.

$BE(d_j, d_e, \varepsilon, t)$ represents the breakage efficiency term:

$$BE(d_i, d_e, t) = \exp\left[-\frac{1}{c_1}\left(\frac{E_c + E_v}{e}\right)\right] \tag{A6}$$

where quantity "*e*" is the kinetic energy of an eddy, E_c is the formation energy, and E_v is the viscous force energy computed by:

$$E_v = b\left(\frac{\pi}{6}\varepsilon^{1/3} d_i^{7/3}\right)\mu_d \sqrt{\frac{\rho_c}{\rho_d}} \tag{A7}$$

where *b* is a constant need to be calibrated. The details of all terms can be found in our prior paper (Zhao et al. 2014b).

Appendix B: The equations for Large Eddy Simulations

The filtered Navier-Stokes Equations for Large Eddy simulations are given by:

$$\frac{\partial \rho_m}{\partial t} + \nabla \cdot (\rho_m \tilde{u}) = 0 \tag{B1}$$

and

$$\frac{\partial (\rho_m \tilde{u})}{\partial t} + \nabla \cdot (\rho \tilde{u} \otimes \tilde{u}) = -\nabla \bar{p} + \nabla \cdot \tilde{\tau} - \nabla \cdot \left(\rho_m \tau^{SGS} \right) + F_{st} - g \cdot x \nabla \rho_m \tag{B2}$$

where ρ_m is the mixture density, $\tilde{u}$ is the mixture velocity, g is the gravity, x is the position vector, $\bar{p}$ is the resolved pressure excluding hydrostatic pressure, $\tilde{\tau}$ is the resolved shear stress and calculated by $\tilde{\tau} = 2\nu_m \bar{S}$, where the mixture kinematic viscosity $\nu_m = \frac{\mu_m}{\rho_m}$, μ_m is the absolute viscosity of the mixture, and $\bar{S} = \frac{1}{2}(\nabla \tilde{u} + \nabla \tilde{u}^T)$ is the strain-rate tensor. The density and dynamic viscosity of air-water mixture is calculated based on the volume fraction of each phase:

$$\rho_m = \rho_{air} \alpha_{air} + \rho_{water} \alpha_{water} \tag{B3}$$

and

$$\mu_m = \mu_{air} \alpha_{air} + \mu_{water} \alpha_{water} \tag{B4}$$

where α_{air} and α_{water} represent the volume fraction of oil and water, respectively. Note that $\alpha_{air} + \alpha_{water} = 1$.

The sub-grid shear stress, $\tau_{ij}^{SGS} = \overline{u_i u_j} - \bar{u}_j \bar{u}_i$ obtained as a result of the filtering operation, can be estimated using SGS modeling. The deviatoric part of SGS stress can be modeled as a function of the strain rate of the resolved velocity field through the Boussinesq hypothesis:

$$\tau_{ij}^{SGS} - \frac{1}{3} \tau_{kk}^{SGS} \delta_{ij} = -2\nu_{SGS} \bar{S}_{ij} \tag{B5}$$

where δ_{ij} is the Kronecker delta, ν_{SGS} is the SGS eddy viscosity, and τ_{kk}^{SGS} is the isotropic part of the sub-grid scale stress.

The transport of oil plumes can be modeled through modified advection diffusion equations, given by:

$$\frac{\partial n(d_i,x,t)}{\partial t}+\nabla\cdot\left[\tilde{u}(x,t)n(d_i,x,t)\right]-\nabla^2\left[\nu^{SGS}(d_i,x,t)\right] + w_{r,i}\mathbf{e}_3\frac{\partial n(d_i,x,t)}{\partial z}=S_i \tag{B6}$$

Here $n(d_i,x,t)$ is the number concentration of droplets with diameter d_i at a given time and position. The second term on the left-hand side represents the advection of droplets with the mixture velocity. The third term on the left-hand side represents the diffusion of oil in water which is induced by the sub-grid eddy viscosity and gradient of oil concertation. The fourth term represents the rise and settling of oil droplets due to their slip velocity relative to the fluid mixture. The source term S_i accounts for droplet breakage and coalescence and is provided by the VDROP model.

The above equations (Eq. (B1) to (B6)), coupled with the VDROP model, simultaneously simulate wave hydrodynamics, oil droplet transport, and the evolution of the droplet size distribution (DSD), thereby capturing the dispersion of oil under wave conditions.

Abbreviations and Acronyms

Short Form	Long Form
ADV	Acoustic Doppler velocimeter
AMOP	Arctic and Marine Oilspill Program
ANS	Alaska North Slope
ASTM	American Society for Testing and Materials
BFT	Baffled flask test
BIO	Bedford Institute of Oceanography
BSEE	Bureau of Safety and Environmental Enforcement
CFD	Computational fluid dynamics
DE	Dispersant effectiveness
DOI	Department of the Interior
DOR	Dispersant-to-oil ratio
DSD	Droplet size distribution
EPA	U.S. Environmental Protection Agency
HPC	High-performance computing
IFT	Interfacial tension
LES	Large-eddy simulation
LISST	Laser In-Situ Scattering and Transmissometry
MLD	Mixed layer depth
OSPD	Oil Spill Preparedness Division
PBM	Population balance model
PIV	Particle image velocimetry
RPM	Revolutions per minute
SGS	Sub-grid scale
VOF	Volume of fluid

Department of the Interior (DOI)
The Department of the Interior protects and manages the Nation's natural resources and cultural heritage; provides scientific and other information about those resources; and honors the Nation's trust responsibilities or special commitments to American Indians, Alaska Natives, and affiliated island communities.

Marine Minerals Administration (MMA)
The mission of the Bureau of Safety and Environmental Enforcement works to promote safety, protect the environment, and conserve resources offshore through vigorous regulatory oversight and enforcement.

MMA Oil Spill Preparedness Program
MMA administers a robust Oil Spill Preparedness Program through its Oil Spill Preparedness Division (OSPD) to ensure owners and operators of offshore facilities are ready to mitigate and respond to substantial threats of actual oil spills that may result from their activities. The Program draws its mandate and purpose from the Federal Water Pollution Control Act of October 18, 1972, as amended, and the Oil Pollution Act of 1990 (October 18, 1991). It is framed by the regulations in 30 CFR Part 254 – *Oil Spill Response Requirements for Facilities Located Seaward of the Coastline*, and 40 CFR Part 300 – *National Oil and Hazardous Substances Pollution Contingency Plan*. Acknowledging these authorities and their associated responsibilities, MMA established the program with three primary and interdependent roles:

- Preparedness Verification,
- Oil Spill Response Research, and
- Management of Ohmsett - the National Oil Spill Response Research and Renewable Energy Test Facility.

The research conducted for this Program aims to improve oil spill response and preparedness by advancing the state of the science and the technologies needed for these emergencies. The research supports the Bureau's needs while ensuring the highest level of scientific integrity by adhering to BSEE's peer review protocols. The proposal, selection, research, review, collaboration, production, and dissemination of OSPD's technical reports and studies follows the appropriate requirements and guidance such as the Federal Acquisition Regulation and the Department of Interior's policies on scientific and scholarly conduct.